Applied Energy 277 (2020) 115576

Contents lists available at ScienceDirect

Applied Energy

journal homepage: www.elsevier.com/locate/apenergy

On the modelling of an Acid/Base Flow Battery: An innovative electrical energy storage device based on pH and salinity gradients

Andrea Culcasi, Luigi Gurreri, Andrea Zaffora, Alessandro Cosenza, Alessandro Tamburini*, Giorgio Micale

Dipartimento di Ingegneria, Università degli Studi di Palermo (UNIPA), Viale delle Scienze Ed.6, 90128 Palermo, Italy

HIGHLIGHTS

- The potential of acid-base flow batteries is addressed.
- A fully-integrated multi-scale model is presented for the first time.
- The model is validated by experimental data purposely collected.
- Main detrimental phenomena are quantified and parasitic currents were the worst.
- Suitable geometries and operating conditions can enhance Round Trip Efficiencies.

ARTICLE INFO

Keywords:
Electrochemical energy storage
Electrodialytic battery
Ion-exchange membrane
Water splitting
Process modelling
Ionic shortcut currents

ABSTRACT

Electrical energy storage can enhance the efficiency in the use of fluctuating renewable sources, e.g. solar and wind energy. The Acid/Base Flow Battery is an innovative and sustainable process to store electrical energy in the form of pH and salinity gradients via electrodialytic reversible techniques. Two electromembrane processes are involved: Bipolar Membrane Electrodialysis during the charge phase and its opposite, Bipolar Membrane Reverse Electrodialysis, during the discharge phase. For the first time, the present work aims at predicting the performance of this energy storage device via the development of a dynamic mathematical model based on a multi-scale approach with distributed parameters. Four models, each one at a different scale, are fully integrated in a comprehensive process simulator. The model was preliminary validated by a comparison with experimental data and a good agreement was found. A sensitivity analysis was performed to identify the most detrimental phenomena. Results indicate a loss of 25–35% of Round Trip Efficiency caused by parasitic currents in the manifolds. Therefore, they may represent the main limit to the present technology performance in scaled-up stacks converting more power. Suitable geometries and operating conditions should be adopted to tackle this issue (e.g. isolated blocks), thus enhancing the battery Round Trip Efficiency.

1. Introduction

In last decades, the demand of renewable energy is rapidly increasing [1] together with the interest in finding energy storage technologies for efficient and robust supply chains [2]. Suitable storage systems should be flexible enough in managing the energy surplus, enabling a usage from kWh scale to MWh scale. Furthermore, they should satisfy some criteria, such as safety, sustainability, durability, economic competitiveness and site-independence. Electrical energy storage technologies can be classified on the basis of the form of the stored energy [3]. Flow batteries store the energy in the electrolyte flowing through the device [4] (Vanadium Redox Flow Batteries are the mostly studied so far [5]) and could satisfy all the above mentioned criteria. However, they still suffer from high costs and environmental issues [6].

1.1. Acid/Base Flow Battery

The Concentration Gradient Flow Battery (CGFB) is an innovative electrodialytic battery that uses hazardless NaCl solutions at different salinity as storage vehicles processed in units provided with monopolar ion-exchange membranes [7]. The salinity gradients are generated during the charge phase by Electrodialysis (ED), and are converted by a controlled mixing (selective transport through the membranes) during

* Corresponding author at: Dipartimento di Ingegneria, Università degli Studi di Palermo (UNIPA), Viale delle Scienze Ed. 6, 90128 Palermo, Italy.
E-mail address: alessandro.tamburini@unipa.it (A. Tamburini).

https://doi.org/10.1016/j.apenergy.2020.115576
Received 23 January 2020; Received in revised form 9 July 2020; Accepted 19 July 2020

Nomenclature

Symbols

a(mol m^{-3}) ion activity
a_1(–) first Darcy friction factor correlation coefficient
a_2(–) second Darcy friction factor correlation coefficient
a_3(–) third Darcy friction factor correlation coefficient
a_4(–) fourth Darcy friction factor correlation coefficient
b(m) spacer width
b_1(–) first Sherwood number correlation coefficient
b_2(–) second Sherwood number correlation coefficient
c_1(–) first local loss coefficient correlation
c_2(–) second local loss coefficient correlation
C(mol m^{-3}) molar concentration
d(m) membrane/channel thickness
d_{ext}(m) pipeline diameter
d_{man}(m) manifold diameter
D(m^2 s^{-1}) diffusion coefficient
E(V) triplet electromotive force corrected for concentration polarization
EMF(V) triplet electromotive force
f(–) frictional coefficient
f_s(–) spacer shadow factor
F(C mol^{-1}) Faraday constant
G(kg m^{-2} s^{-1}) mass flux
GPD(W m^{-2}) gross power density
i(A m^{-2}) current density
I(A) current intensity
J(mol m^{-2} s^{-1}) molar flux
k(–) generic local loss coefficient
k_ζ(–) regression coefficient
l_{man}(m) triplet thickness
l_{oma}(m) length of the spacer regions out of the active area
L(m) spacer length
(m) pipeline length
L_p(ml m^{-2} h^{-1} bar) osmotic permeability
L_x(m) half channel length
M(g mol^{-1}) molar mass
n(–) number of ion species
n_h(–) hydration number
N(–) number of triplets
N_{holes}(–) number of inlet spacer holes
NPD(W m^{-2}) net power density
P(Pa) pressure
PPD(W m^{-2}) pumping power density
Q(m^3 s^{-1}) volume flow rate
R(Ω) generic electric resistance
R_g(J mol^{-1} k^{-1}) gas constant
Re(–) Reynolds number
RTE(–) Round Trip Efficiency
Sc(–) Schmidt number
Sh(–) Sherwood number
t(s) time
t_c(s) charge time
t_d(s) discharge time
t_i(–) ion transport number
T(K) temperature
u(m s^{-1}) mean flow velocity
U potential difference over the series of resistances R_u and R_{bl}
U_{ext} potential difference over the external load R_u
ΔV(V) generic voltage difference
V_t(m^3) solution volume in the tank
x(m) coordinate along the flow direction
X(mol m^{-3}) membrane fixed charge groups
z(–) ion charge

Greek letters

ζ(–) generic physical property
η_{BL}(V) boundary layer potential drop
θ(–) polarization coefficient
μ(Pa s) dynamic viscosity
π_{osm}(bar) osmotic pressure
ρ(kg m^{-3}) mass density
σ(S m^{-1}) electric conductivity
χ(–) pump efficiency

Subscripts/superscripts

a acid
av average
AEM anionic exchange membrane
AEL anionic exchange layer
b base
bl blank
BPM bipolar membrane
c collector
ch channel
co co-ion
ct counter-ion
CEM cationic exchange membrane
CEL cationic exchange layer
d distributor
diffusive
down lower branch
e. osm electro-osmotic
ext external
fd fully developed
h electric current
i ion species
in inlet
int interface
IEL ionic exchange layer
IEM ionic exchange membrane
j ion species
k generic cell-triplet in the stack
l local
loss loss
m membrane
man manifold
nopar reference case neglecting shunt currents
ohm Ohmic
out outlet
oma out of the membrane active area
osm osmotic
s salt
sol solution
spacer spacer
split/recomb Water flux through the BPM
t tank
tot total
u external load
up upper branch
w water
x longitudinal branch (*up* or *down*)

Acronyms/abbreviations

AB-FB	Acid Base-Flow Battery
AEL	Anion-Exchange Layer
AEM	Anion-Exchange Membrane
BMED	Bipolar-Electrodialysis
BMRED	Bipolar-Reverse Electrodialysis
BPM	BiPolar Membrane
CEL	Cation-Exchange Layer
CEM	Cation-Exchange Membrane
CFD	Computational Fluid Dynamic
CGFB	Concentration Gradient Flow battery
ED	Electrodialysis
LCOS	Levelized Cost of Storage
OCV	Open Circuit Voltage
RED	Reverse Electrodialysis
RTE	Round Trip Efficiency
SOC	State Of Charge

the discharge phase by Reverse Electrodialysis (RED) to return electrical energy [8]. ED is a well-known desalination technique used for water desalination [9], municipal [10] and industrial [11] wastewater treatment, and other purposes in chemical, biochemical, food and pharmaceutical processes, including industrial applications. RED is the opposite process, where the salinity gradient between two solutions, is used to harvest electricity [12]. Prototypal installations in real life environments have been carried out so far [13]. The ED-RED coupling within the CGFB is currently installed as pilot scale device at The Green Village (Delft, The Netherlands), coupled to a photovoltaic system with an expected power-to-energy ratio of 0.1 (i.e. 1 kW vs 10 kWh) [14]. The theoretical energy density of the electrolyte solutions is in the order of 1 kWh m^{-3}, much lower than that of Vanadium Redox Flow Battery (up to ~35 kWh m^{-3} [15]).

The energy density can be enhanced by adding a bipolar membrane (BPM), thus allowing for the storage of energy in the form of acid, base and saline solutions (i.e. pH and salinity gradients). This system, called Acid/Base Flow Battery (AB-FB, Fig. 1), could represent an innovative, safe and sustainable way to store energy with high performance [16]. The AB-FB is an electrodialytic battery based on the reversible water dissociation. In particular, the Bipolar Membrane Electrodialysis (BMED) process uses electrical energy to produce acidic and alkaline solutions that are then exploited in the reverse process, i.e. the Bipolar Membrane Reverse Electrodialysis (BMRED) to generate electricity.

BMED has a multitude of potential applications for acid/base production/regeneration [17]. The BPM is made by a cation exchange layer and an anion exchange layer, which promote catalytically the water dissociation in the interlayer under the effect of an electric field, thus releasing protons and hydroxyl ions [18]. The BMED stack is one of the reaction units of the AB-FB. It is composed by a number of repetitive units called triplets which, in turn, consist of an anion- and a cation-exchange (monopolar) membrane (AEM and CEM, respectively) and a BPM separated by net spacers. These create the channels where the electrolyte solutions (i.e. acid, base and salt) flow. During the charge phase (BMED), water dissociation occurs inside the BPM, whilst during the discharge phase (BMRED) the neutralization reaction takes place, as schematically shown in Fig. 2a and b.

1.2. State of the art

Theoretically, an energy density of about 11 kWh m^{-3} can be stored in 1 M acidic and alkaline solutions, although a measured energy density of 2.9 kWh m^{-3} was reported by van Egmond et al. [16]. However, this value is comparable with those obtained with Pumped Hydroelectric Systems (0.5–2 kWh m^{-3}) and Compressed Air Energy Storage systems (2–6 kWh m^{-3}) that are, on the other hand, strongly site-dependent technologies [3]. Compared to Li-ion or Lead-Acid batteries, the AB-FB suffers of a lower energy density (200–620 kWh m^{-3} for Li-ion battery and 30–90 kWh m^{-3} for Lead-Acid battery), but it is designed to work with discharge times of hours delivering powers in the order of MWs, whilst the former ones have discharge times of minutes and delivered powers in the kW - MW range [19]. The potential Levelized Cost of Storage (LCOS) of AB-FBs (0.44 € kWh^{-1}) would be lower than that estimated for Li-ion batteries (0.61 € kWh^{-1}) but higher than that calculated for Lead-Acid batteries (0.29 € kWh^{-1}) [20].

By testing commercial membranes [21] or custom membranes [22], pioneering studies highlighted the need of high-selective membranes to implement real applications of the AB-FB concept. After several years in which this interesting technology has been almost ignored, more recently some researchers have carried out some studies. Kim et al. [23] reported stable efficiencies over nine cycles, but the operation cyclability was then seriously compromised. This behaviour was attributed to the protons leakage from the acid chamber to the salt and electrode chambers (single-cell experiments). Nine stable cycles were performed in a single-cell unit also by van Egmond et al. [16] who measured a power density of 3.7 W m^{-2} per membrane and a round-trip efficiency up to 13.5%, with an energy density up to 2.9 Wh kg^{-1}, as mentioned above. The coulombic efficiencies were moderate (13–27%), mainly due to unwanted protons and hydroxyl ions transport, which caused an energy loss of ~50%. Moreover, a high internal resistance caused low voltage efficiencies (~50%). Interestingly, during the discharge phase the current density was limited at 15 A m^{-2} by delamination (or ballooning) issues, due to a recombination rate of protons and hydroxyl ions higher than the diffusion of the produced water. In order to enhance the power density and the process efficiency, suitable tailor-made membranes are needed.

A similar general conclusion can be drawn from the experimental results by Xia et al. [24] (one-cell unit, 20 cycles). Moreover, the AB-FB performance could be theoretically enhanced by using higher acid/base concentrations (1 M was the "standard" maximum used so far), thus requiring further improved transport properties of the membranes. Another important aspect concerns the need to process larger volumes of the electrolyte solutions in order to convert higher amounts of energy, thus requiring the use of batteries with a higher number of triplets (repetitive units). In such stacks, additional phenomena affecting the process performance arise, namely shunt currents via manifolds [25]. Therefore, some measures have to be taken in the design of scaled-up units, e.g. the implementation of serial flow layouts with isolated blocks.

In order to promote the techno-economic competitiveness of the AB-FB, validated modelling tools can be very useful to assess the process

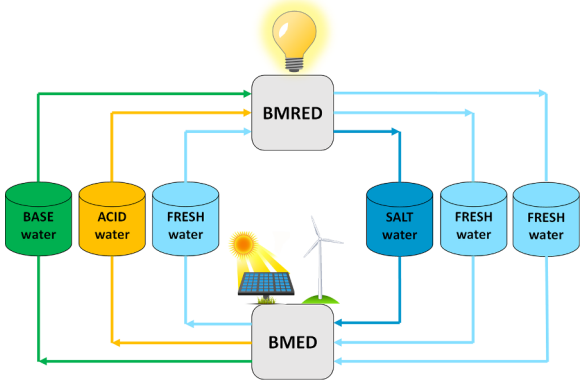

Fig. 1. Acid/Base Flow Battery scheme.

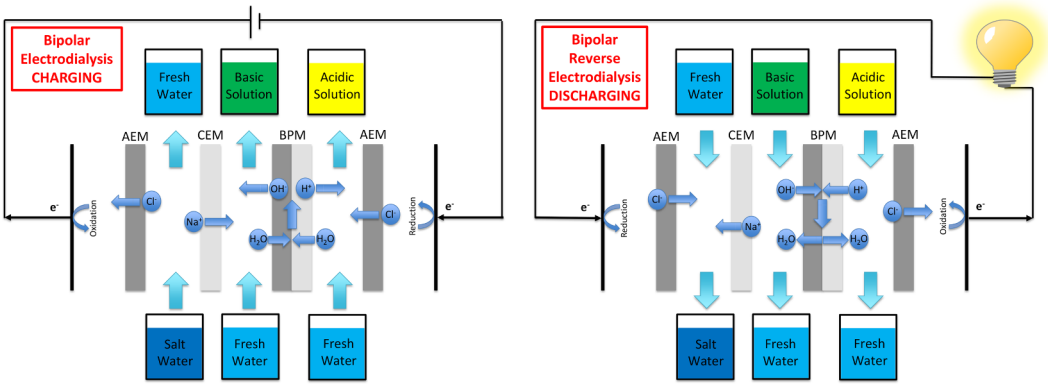

Fig. 2. Charging a) and discharging b) operation of the Acid/Base Flow Battery.

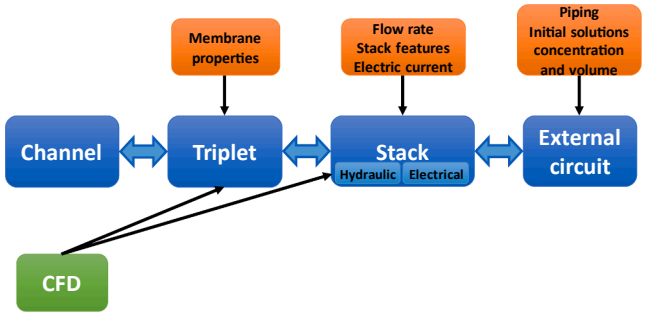

Fig. 3. Multi-scale model scheme. The dark blue boxes indicate the four dimensional scales of the model, which interact each other and are integrated in a single tool. Light blue boxes indicate the two stack sub-models. Orange boxes report the main input parameters. Correlations for flow and mass transfer characteristics coming from Computational Fluid Dynamics (CFD) simulations are used as input for the triplet simulation and the stack hydraulic sub-model.

performance and to drive the design and optimization. However, to the authors' knowledge, no studies have been devoted so far to the modelling of AB-FBs. On the other hand, the phenomenology taking place in an electrodialytic battery with BPMs is very complex, as it includes fluxes of different kind for several ion species and for water, electrochemical equilibria, Ohmic and non-Ohmic voltage drops, and hydrodynamics. Moreover, the behaviour of an AB-FB is intrinsically transient. In order to simulate such complex systems, multi-scale models can be suitable. Previous works showed the effectiveness of multi-scale tools in providing reliable and accurate predictions, both for ED [26] and RED [27] processes, requiring only empirical data on the membrane properties.

In this work, a process model able to describe the main phenomena involved in AB-FB systems was developed following a multi-scale approach, thus providing a tool useful to guide the battery design. The multi-scale model is with distributed parameters and is composed of four sub-models. Each sub-model is related to a different scale, starting from the lowest one represented by the channel between two membranes and ending with the highest scale represented by the external hydraulic circuit. Moreover, the sub-models interact each other. Once the model has been validated with experimental data purposely collected, it was used to assess the impact of the main detrimental phenomena on the battery performance. This work falls within the framework of the BAoBaB project [28].

2. Mathematical modelling

Many irreversibility sources are responsible for the reduction of the process efficiency. Some of them are associated to the non-ideal transport properties of the ion exchange membranes, others are correlated to geometric features of the stack and operating conditions. With particular reference to the second group, the main issues for internal losses in ED/RED units may be identified in Ohmic and non-Ohmic voltage drops, pressure drops, and concentration polarization phenomena. In addition, ionic shortcut currents via manifolds, known also as parasitic or shunt currents, or current leakages, may arise in stacks with a large number of repetitive cells where the electrical resistance of the parasitic pathways is comparable with the cell resistance in the (desired) direction perpendicular to the membranes [27]. This can happen in BMED/BMRED stacks, thus affecting the efficiency of an AB-FB as well [25], as mentioned above.

Note that the various phenomena involved in the internal losses are of different nature and scale but related each other, thus single separate models can only provide partial predictions. On the other hand, an integrated mathematical multi-scale model is the most effective tool to simulate all these phenomena and their interactions at the same time. With specific reference to the shunt currents, suitable models simulating the electrical behavior of the stack are needed in order to have reliable predictions [27]. Therefore, a comprehensive AB-FB process simulator based on a multi-scale structured simulation strategy was developed in this work.

The multi-scale process model is divided into four dimensional scales or levels, each of them is simulated by its specific sub-model(s), requiring some inputs, as schematically shown in Fig. 3. The unidirectional black arrows indicate towards what model-scale the input parameters are sent to. The bidirectional blue arrows indicate how the model levels communicate with each other. The channel-scale is the lowest level, the triplet is the medium-low scale, the stack is the middle-high scale and, finally, the external hydraulic circuit outside the stack is the highest level. The channel modelling level computes the physical properties of the solutions by correlations from different database. The triplet is simulated by a sub-model which calculates ions and water fluxes through the membranes, electrochemical equilibria, mass balances (and thus concentrations and flow rates), electromotive force, and triplet resistance. The main inputs that this sub-model requires are the membrane properties, as well as the flow layout (co- or counter-flow). Then, two sub-models that solve the equivalent hydraulic circuit and the electrical one, respectively, compose the stack modelling level, thus predicting the distribution of pressure, flow rate and electric current, along with the power provided to/by the stack and the Round Trip Efficiency (RTE). The inputs used at this level of simulation are the flow rate of the solutions, the stack features (number of triplets, spacer-filled channel geometry, blank resistance) and the external electric current. Finally, the external hydraulic circuit is the highest hierarchical level of the model, which calculates dynamic mass balances in the tanks, and pressure drops, pumping power and net power of the whole system. The piping features and the initial solutions concentration and volume are imposed as input.

The model is with distributed parameters. Each channel and each triplet are discretized in one dimension (along the flow direction). The hydraulic and electric sub-models for the stack simulate explicitly all the channels and the triplets of the AB-FB unit connected by manifolds, thus they can be considered with distributed parameters as well, though the equivalent circuits have a lower discretization degree with respect to that used in the channel and triplet sub-models.

Remember that the process simulated, i.e. the AB-FB, is an electrical energy storage system, thus its operation is transient. The electrolyte solutions can be simply recirculated continuously to the tanks or can be fed to the stack with multiple-passage operations. Moreover, the battery has to work for a number of charge/discharge cycles. The present process model can simulate all these features. A quasi-steady state approach is adopted to model the battery. Particularly, all the dimensional scales except the external circuit are simulated with a steady-state approach. Concerning the external circuit, tanks are dynamically modelled.

The algebraic equations and differential equations (mass balances) describing the various sub-models structured in four scales form one single overall equations system. Therefore, all the sub-models are integrated in a single simulation tool, implemented in the gPROMS® process simulator environment. Unlike the more used sequential modular approach, this software presents an advanced equation-oriented structure. The solution of the mathematical problem is obtained by built-in solvers. gPROMS enables the choice of important numerical constraints especially in the iteration process of the nonlinear solvers, e.g. the maximum residual of each equation. A set of parameters was chosen as a compromise between numerical accuracy and computational time. As a result, under steady-state condition, mass balances residuals were always found to be lower than 10^{-11}. This results in a mass balance residual of less than 0.1% for a round-trip cycle.

The model output consists of the distribution of the variables along with the prediction of the performance parameters of the AB-FB system. Therefore, the developed model provides essential information for the unit design (e.g. manifold size, channel size) and for the choice of operating conditions (e.g. current density, flow rates) able to minimize all the detrimental phenomena.

As shown in Fig. 3, the model is completed by Computational Fluid Dynamics (CFD) simulations of spacer-filled channels. CFD results are used in the form of correlations as input data for the triplet sub-model (mass transport) and the stack sub-model (hydraulic friction).

Hereinafter all the sub-models are described in detail.

2.1. CFD model

Three-dimensional finite-volume Computational Fluid Dynamics (CFD) simulations of spacer-filled channels can predict flow and mass transfer characteristics under the assumption of fully developed conditions (periodic unit cell). This modelling approach is intended to simulate regions of the channel being far away from boundaries (inlet, outlet, lateral walls). Details are reported in previous works [29]. Note that water flux is crucial for the functioning of the BPM. However, typical transpiration rates in BPMs are relatively low [30], so that the inclusion of water transpiration in CFD simulations purposely performed had negligible effects on the velocity and concentration fields. Therefore, simpler conventional CFD simulations, where transpiration phenomena are neglected, may be performed and pre-existent correlations can be used.

The following kinds of correlation were adopted for the Darcy friction factor and the Sherwood number:

$$\frac{fRe}{96} = a_1 Re^3 + a_2 Re^2 + a_3 Re + a_4 \quad (1)$$

$$Sh = (b_1 Re + b_2)\left(\frac{Sc}{Sc_{ref}}\right)^{0.5} \quad (2)$$

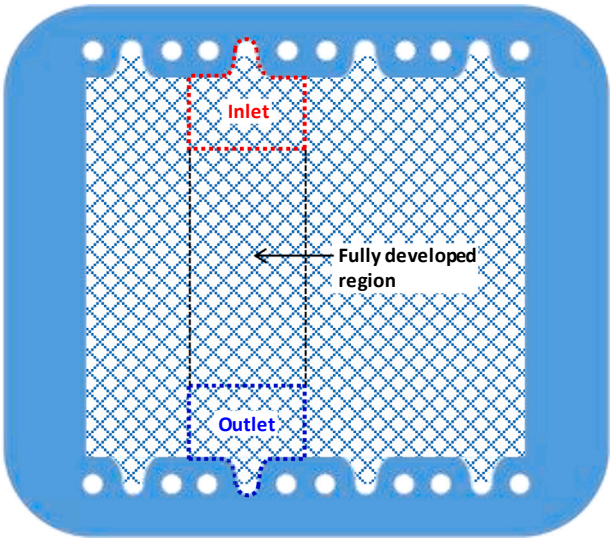

Fig. 4. Net spacer provided with gasket. The computational domains used in the CFD simulations of the inlet/outlet regions are highlighted.

where Re is the Reynolds number, Sc is the Schmidt number, Sc_{ref} is a reference value for the Schmidt number [31] (equal to 615), and the other symbols indicate coefficients depending on the geometry. In the simulations of the AB-FB presented in this work, a woven spacer with 90° angled filaments, pitch to height ratio equal to 2, and flow attack angle of 45° (i.e. flow bisecting the angle between the filaments) was considered. For this configuration, the following values of the coefficients were used ($Re < 30$): $a_1 = -2.1 \cdot 10^{-5}$, $a_2 = 0.0024$, $a_3 = 0.001$, $a_4 = 14.831$, $b_1 = 2.81$, and $b_2 = 14.5$ [32].

Further CFD simulations were aimed at characterizing pressure drops at the inlet/outlet regions of the channels connected to the manifolds. Therefore, larger computational domains with the actual geometry of inlet/outlet regions of spacer-filled channels provided with gasket were simulated. In order to deal with a low computational effort, the net spacer was simply modelled as a continuous porous medium, whose pressure drop features were set using the previous unit cell simulation results. Moreover, one single hole and the associated region were simulated, assuming periodic conditions at the lateral boundaries (see Fig. 4). Notably, a full computational domain including the inlet and outlet manifolds and the whole channel was also built. Corresponding CFD simulations were preliminary carried out and relevant results were compared with those pertaining to the periodic domain. Only very slight differences (maximum discrepancy lower than 4%) were found, thus indicating that adopting a periodic domain is a reliable approach. From this simple modelling approach, the following kind of correlation for the local loss coefficient k_{spacer} was obtained

$$k_{spacer} Re = c_1 Re + c_2 \quad (3)$$

where the coefficients c_1 and c_2 depend on the geometry. For example, for a spacer with a shape as that reported in Fig. 4, with manifolds diameter $d_{man} = 8$ mm and 7 inlet/outlet holes in 25 cm of width, the values of the coefficients were: $c_1 \approx 2{,}400$ and $c_2 \approx 166{,}000$ ($Re < 30$). Note that at the low Reynolds numbers typical for RED systems, there is only a small discrepancy from an in-out symmetric behaviour, i.e. the local loss coefficients k_{spacer} (and thus c_1 and c_2) are the same for inlet and outlet regions.

Correlations reported in Eqs. (1) and (3) are used in the stack hydraulic sub-model, while that reported in Eq. (2) is used in the triplet sub-model.

2.2. Channel model

The channel is the lowest level of the multi-scale model. Here,

physical properties of the three electrolyte solutions are evaluated in all the channels of the stack. The channel model was implemented with a 1-D discretization of all the considered variables. 30 discretization intervals were found to be more than sufficient to guarantee a good accuracy of the numerical resolution of the model. Although a higher number of intervals would increase the accuracy of a few percentage (e.g. < 2% with 50 intervals), it strongly increment the computation time. The inlet variables such as the channel inlet flow velocity and ion concentrations, are time-dependent and function of the solutions exiting the external tanks. Each time step is 100 s.

HCl, NaOH and NaCl are the electrolyte considered in this work. However, the co-ion transport causes the presence of several ion species in each channel, instead of a single electrolyte. Mass density is calculated following Laliberté's model [33]. Ion activity and osmotic coefficients are evaluated adopting the Pitzer virial equations for multi-electrolyte solutions. Particularly, some of the used parameters are related to the pure species [34], others to the mixtures [35]. The electrical conductivity, dynamic viscosity and the ions diffusivity in solution are evaluated from correlations derived from linear regression of simulations results by OLI Studio®.

2.3. Triplet model

At the middle-low level of simulation, the triplets are simulated by a stationary, one-dimensional model, with the same spatial discretization degree as that of the channel. The inlet variables such as the channel inlet flow velocity and ion concentrations, are time-dependent and function of the solutions exiting the external tanks. Each time step is 100 s. Fig. 5 shows a scheme of a triplet, where each membrane can be crossed by ion (Ohmic and diffusive) transport and water (osmotic and electro-osmotic) transport. The membrane-solution interfaces 1 (left) and 2 (right) are indicated for each channel.

2.3.1. Ions and water fluxes

In order to calculate membrane fluxes, the Nernst-Planck-Donnan approach for multi-ion systems is adopted [36]. The ion transport through the membrane is given by the sum of the diffusive and Ohmic terms and follows the general expression

$$J_{i,m} = -\sum_j D_{i,j,m}\nabla C_{j,m} + \frac{t_{i,m} i}{z_i F} \tag{4}$$

in which $J_{i,m}$ is the total molar flux of the i-th ion across the generic membrane m (i.e. CEM, AEM or BPM), $D_{i,j,m}$ is the cross-diffusion coefficient (defined later), $C_{j,m}$ is the concentration in the membrane phase of the j-th ion, $j = 1, 2, \cdots, n$ (where n is the number of ion species), $t_{i,m}$ is the transport number of the i-th ion within the membrane, i is the current density, z_i is the ion charge and F is the Faraday constant. $J_{i,m}$ is positive if entering the channel, negative if exiting the channel. Current density i is positive during the charge step, while it is negative during the discharge step. Note that the Nernst-Plank approach is strictly valid for diluted electrolytes. A rigorous approach including activity would require the adoption of the Stefan-Maxwell equation which cannot be used without the availability of the cross-phenomenological coefficients taking into account ion-ion interactions. These coefficients could be assessed only by carrying out suitably devised experiments. This is why the Nernst-Plank approach, although less rigorous, is the one commonly used [37].

According to Eq. (4), the overall Ohmic fluxes of the species i across the two membranes bounding the three compartments can be calculated as

$$J_{ohm,i,a} = \frac{(t_{i,CEL} - t_{i,AEM})i}{z_i F} \tag{5}$$

$$J_{ohm,i,b} = \frac{(t_{i,CEM} - t_{i,AEL})i}{z_i F} \tag{6}$$

$$J_{ohm,i,s} = \frac{(t_{i,AEM} - t_{i,CEM})i}{z_i F} \tag{7}$$

where $J_{ohm,i,a}$, $J_{ohm,i,b}$, $J_{ohm,i,s}$ are the overall Ohmic fluxes of each acid, base and salt channels respectively, $t_{i,CEL}$, $t_{i,AEL}$, $t_{i,CEM}$, $t_{i,AEM}$ are the transport numbers of the i-th ion in the cation and anion exchange layers of the bipolar membrane and in the cation and anion exchange membranes, respectively. $J_{ohm,i,sol}$ are positive if entering the channels, negative otherwise. The ion transport numbers in the membranes are related to the ion diffusion coefficients of all the ions and to the average ion concentration within the membrane by the expression

$$t_{i,m} = \frac{z_i^2 D_{i,m} \bar{C}_{i,m}}{\sum_j z_j^2 D_{j,m} \bar{C}_{j,m}} \tag{8}$$

in which $D_{i,m}$ is the diffusion coefficient of the i-th ion, and $\bar{C}_{i,m}$ is the average ion concentration within the membrane. $D_{i,m}$ is a parameter of the model reported in Table A.1. Preliminary data of ion diffusivities were estimated empirically by performing experiments with a two-chambers diffusion cell. $\bar{C}_{i,m}$ is calculated from the membrane-solution interface concentrations on both membrane sides, which in turn depend on the Donnan equilibrium between the two phases. The following n-1 Donnan equilibrium equations at the membrane-solution interfaces are applied

$$\frac{R_g T}{z_i F} ln \frac{C_{i,sol,int}}{C_{i,m,int}} = \frac{R_g T}{z_{i+1} F} ln \frac{C_{i+1,sol,int}}{C_{i+1,m,int}} \tag{9}$$

where $C_{i,sol,int}$ and $C_{i,m,int}$ are the ion concentrations at the interface on the solution and membrane side, respectively, R_g is the gas constant and T is the temperature. Eq. (9) can be applied for i in the interval [1;n-1]

Moreover, the electro-neutrality within the membrane is considered with the general expression:

$$X + \sum C_{co,m} = \sum C_{ct,m} \tag{10}$$

where X is the fixed charge group concentration in the IEM, $C_{co,m}$ and $C_{ct,m}$ are the co-ion and counter-ion concentrations in the membrane phase.

According to the diffusion-conduction equation Eq. (4), the diffusive flux of the ion species i through a membrane m is

$$J_{diff,i,m} = -\sum_j D_{i,j,m}\nabla C_{j,m} \tag{11}$$

where the concentration gradients are calculated by solving the Donnan equilibrium expressions, and the cross-diffusion coefficients $D_{i,j,m}$ are expressed as follows:

$$D_{i,j,m} \equiv D_{i,m}\delta_{ij} + \frac{t_{i,m}}{z_i} z_j (D_{i,m} - D_{j,m}) \tag{12}$$

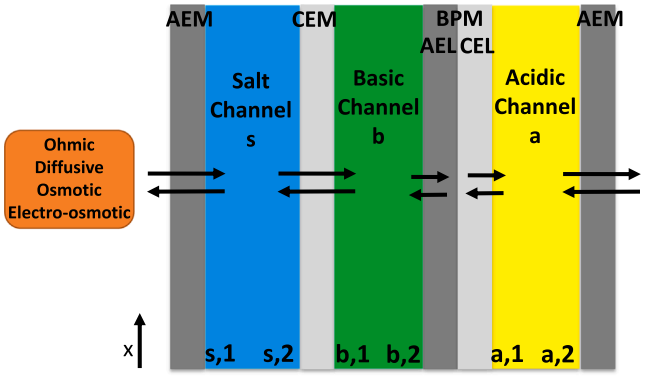

Fig. 5. Scheme of the triplet (with an additional CEM). All the possible fluxes of ions and water through the membranes are listed. The membrane-solution interfaces in each channel are indicated as *sol,1* (on the left) and *sol,2* (on the right), being *sol* either salt (s), basic (b) or acid (a) solution.

Table A1
List of the physical properties in the acid (a), base (b) and salt (s) solution and the regression coefficients used to compute them by Equation (A.1).

	ζ	sol	i	j	$k_{\zeta,sol,1}$	$k_{\zeta,sol,2}$	$k_{\zeta,sol,3}$
Electrical conductivity (S m^{-1})	σ	a	H^+	Na^+	0.0341	0.00646	0.908
	σ	s	H^+	–	0.0353	0	2.52
	σ	b	OH^-	Cl^-	0.0184	0.00697	0.772
Dynamic viscosity (Pa s)	μ	a	H^+	–	2.8E−9	0	0.928E−3
	μ	s	H^+	–	2.8E−9	0	0.928E−3
	μ	b	OH^-	–	0.215E−6	0	0.927E−3
Ion diffusivity (m s^{-2})	D_H	a	H^+	–	−1E−13	0	2E−9
	D_{Na}	a	Na^+	–	−5E−14	0	1E−9
	D_{OH}	a	OH^-	–	0	0	4E−9
	D_{Cl}	a	Cl^-	–	−7E−14	0	2E−9
	D_H	s	H^+	–	−1E−13	0	2E−9
	D_{Na}	s	Na^+	–	−5E−14	0	1E−9
	D_{OH}	s	OH^-	–	−1E−13	0	5E−9
	D_{Cl}	s	Cl^-	–	−7E−14	0	2E−9
	D_H	b	H^+	–	0	0	8E−9
	D_{Na}	b	Na^+	–	−2E−13	0	1E−9
	D_{OH}	b	OH^-	–	−5E−13	0	5E−9
	D_{Cl}	b	Cl^-	–	−2E−13	0	2E−9

where δ_{ij} is the Kronecker delta.

The total i-th ion flux across the two membranes bounding each channel $J_{tot,i,sol}$ is calculated as the sum of the overall Ohmic contribution (Eqs. (5)–(7)) and the two diffusive contributions

$$J_{tot,i,sol} = J_{ohm,i,sol} + J_{diff,i,m,1} + J_{diff,i,m,2} \tag{13}$$

in which $J_{diff,i,m,1}$ and $J_{diff,i,m,2}$ are the diffusive fluxes across the left (1) and right (2) membranes bounding the channel.

The osmotic fluxes are generated by the osmotic pressure difference across the membrane. In formulae:

$$G_{osm,a} = \frac{\rho_w L_p (\pi_{osm,a,2} - \pi_{osm,s,1})}{3.6 \cdot 10^9} \tag{14}$$

$$G_{osm,b} = \frac{\rho_w L_p (\pi_{osm,b,1} - \pi_{osm,s,2})}{3.6 \cdot 10^9} \tag{15}$$

where $G_{osm,a}$, $G_{osm,b}$ are the osmotic mass fluxes of the acid and base channels, expressed in kg m^{-2} s^{-1}, ρ_w is the water mass density at 25 °C in kg m^{-3}, L_p is the Osmotic permeability (expressed in ml m^{-2} h^{-1} bar^{-1}), $\pi_{osm,a,2}$, $\pi_{osm,s,1}$, are osmotic pressures at the left and right side respectively of the AEM and $\pi_{osm,b,1}$, $\pi_{osm,s,2}$ are those of the CEM (all expressed in bar). $G_{osm,sol}$ is negative when entering the channel, positive otherwise.

The electro-osmotic fluxes represent the number of molecules entrained by the solvation shell of each ion passing across the IEMs. These fluxes can be calculated as

$$G_{e.osm,sol} = 10^{-3} M_{H_2O} \sum_i J_{tot,i,sol} n_{h,i} \tag{16}$$

where M_{H_2O} is the molar mass of water in g mol^{-1} and $n_{h,i}$ is the number of water molecules with the solvation shell per each ion (considered equal to 1 for H^+ and OH^- [38], 6 for Na^+ and 8 for Cl^- [39]). $G_{e.osm,sol}$ is positive when entering the channel, negative otherwise.

In the acid and base compartments, the stoichiometric water flux through the BPM due to the water dissociation (charge) or acid/base neutralization (discharge) is

$$G_{split/recomb,sol} = -\frac{t_{ct,IEL} i}{2F} M_{H_2O} \cdot 10^{-3} \tag{17}$$

where $t_{ct,IEL}$ is the transport number of the counter-ion (H^+ or OH^-) in the CEL or AEL of the BPM, respectively $G_{split/recomb,sol}$ is positive when entering the channel, negative otherwise.

The overall water mass fluxes $G_{w,sol}$ (positive when entering the channel, negative otherwise) for the acid and base channels are evaluated according to the equations

$$G_{w,sol} = G_{e.osm,sol} - G_{osm,sol} + G_{split/recomb,sol} \tag{18}$$

The water mass flux for the salt channels is related to the water fluxes calculated for the acid and base compartments

$$G_{w,s} = -G_{w,a} - G_{w,b} \tag{19}$$

2.3.2. Electromotive force and electrical resistance

The electric potential generated across the IEMs in the triplet E can be written as

$$E = EMF + sgn(i)\eta_{BL} \tag{20}$$

where $sgn(i)$ is the algebraic sign of the current density, EMF is the triplet electromotive force that would be generated by the membranes in contact with the bulk solutions, and η_{BL} is the contribution to E due to concentration polarization boundary layers.

The electromotive force is calculated by the general Nernst equation [40]

$$E = \sum_{IEMs} \left(-\frac{R_g T}{F} \int_{left,IEM}^{right,IEM} \sum_{ions} \frac{t_i}{z_i} d\ln a_{int,i} \right) \tag{21}$$

where $a_{int,i}$ is the activity of the i-th ion at the solution side of the membrane-solution interface (i.e. *right*, *IEM* and *left*, *IEM* which are the right and the left side of each membrane as shown in Fig. 5), expressed in mol m^{-3}.

η_{BL} accounts for the non-Ohmic variation of E in a triplet due to the effects of concentration polarization phenomena in the boundary layers on all the six solution-membrane interfaces [31]

$$\eta_{BL} = -\frac{R_g T}{F} \sum_{int} \sum_{ions} \frac{t_i}{z_i} \ln \theta_{i,sol,int} \tag{22}$$

in which $\theta_{i,sol,int}$ are the six polarization coefficients, defined as

$$(\theta_{i,sol,int})^{sgn(J_{diff,i,sol,int})} = \frac{C_{i,sol,int}}{C_{i,sol}} \tag{23}$$

where $C_{i,sol}$ and $C_{i,sol,int}$ are the concentrations of the i-th ion in the *sol* channel (i.e acid, base or salt) in the bulk and at the solution-membrane interface, respectively, and $sgn(J_{diff,i,sol,int})$ is the sign of the diffusive flux of the i-th ion at the interface with the membrane, solution side. Imposing the continuity of the total flux at the interface, it can be calculated as

$$J_{diff,i,sol,int} = J_{diff,i,m} + \frac{(t_{i,m} - t_{i,sol}) i}{F} \tag{24}$$

where $t_{i,sol}$ is the ion transport number in the solution

$$t_{i,sol} = \frac{z_i^2 D_{i,sol} C_{i,sol}}{\sum_j z_j^2 D_{j,sol} C_{j,sol}} \tag{25}$$

in which $D_{i,sol}$ is the ion diffusion coefficient of the i-th ion in the solution. From the definition of the Sherwood number, it follows that the polarization coefficient can be calculated as

$$\theta_{i,sol,int} = \left(1 - \frac{J_{diff,i,sol,int} 2 d_{sol}}{Sh_{sol,int} D_{i,sol} C_{i,sol}} \right)^{sgn(J_{diff,i,sol,int})} \tag{26}$$

where d_{sol} is the spacer thickness and $Sh_{sol,int}$ is the Sherwood number in the considered interface, which is evaluated by CFD correlations (Eq. (2)).

The triplet electric resistance R (in Ω) is calculated as follows

$$R = \sum_{sol} R_{sol} + \sum_m R_m \tag{27}$$

where R_{sol} and R_m are the electrical resistance in the feed channels (i.e.

acid, base and salt) perpendicular to the membranes and the electrical resistance of the membranes (i.e. CEM, AEM and BPM). R_{sol} are calculated as

$$R_{sol} = f_s \frac{d_{sol}}{b\ \Delta x\ \sigma_{sol}} \tag{28}$$

in which f_s is the spacer shadow factor (which can be assumed, for example, equal to the inverse of the volume porosity), b is the channel width, Δx is the length of a discretization interval (e.g. equal to 1/30 of the channel length) and σ_{sol} is the electrical conductivity of the electrolyte solution. In the case of commercial membranes, R_m can be known under specific conditions (composition and concentration of the electrolyte solution) from manufacturers catalogues, otherwise it can be experimentally evaluated, with the advantage to have more detailed information on the membrane behaviour under different conditions.

2.3.3. Mass balances

For each control volume of each channel, one-dimensional co-current mass balance equations are written for each ion species and the electrolyte solution.

Mass balances for the acid channels are:

$$\frac{\partial Q_a C_{Na^+,a}}{\partial x} = b J_{tot,Na^+,a} \tag{29}$$

$$\frac{\partial Q_a C_{Cl^-,a}}{\partial x} = b J_{tot,Cl^-,a} \tag{30}$$

$$\frac{\partial Q_a C_{H^+,a}}{\partial x} = b (J_{tot,H^+,a} - J_{tot,OH^-,a}) \tag{31}$$

$$C_{OH^-,a} = 10^3 10^{\left(-14-\log\frac{C_{H^+,a}}{10^3}\right)} \tag{32}$$

$$\frac{\partial Q_a \rho_a}{\partial x} = (J_{tot,Na^+,a} M_{Na^+} + J_{tot,Cl^-,a} M_{Cl^-} + (J_{tot,H^+,a} - J_{tot,OH^-,a}) M_{H^+}) b \\ 10^{-3} + G_{w,a} b + J_{tot,OH^-,a} M_{H_2O} b 10^{-3} \tag{33}$$

where Q_a is the acid volume flow rate and ρ_a is the acid mass density.

Similar expressions can be written for the salt channels:

$$\frac{\partial Q_s C_{Na^+,s}}{\partial x} = b J_{tot,Na^+,s} \tag{34}$$

$$\frac{\partial Q_s C_{Cl^-,s}}{\partial x} = b J_{tot,Cl^-,s} \tag{35}$$

$$\frac{\partial Q_s C_{H^+,s}}{\partial x} = b (J_{tot,H^+,s} - J_{tot,OH^-,s}) \tag{36}$$

$$C_{OH^-,s} = 10^3 10^{\left(-14-\log\frac{C_{H^+,s}}{10^3}\right)} \tag{37}$$

$$\frac{\partial Q_s \rho_s}{\partial x} = (J_{tot,Na^+,s} M_{Na^+} + J_{tot,Cl^-,s} M_{Cl^-} + (J_{tot,H^+,s} - J_{tot,OH^-,s}) M_{H^+}) b \\ 10^{-3} + G_{w,s} b + J_{tot,OH^-,s} M_{H_2O} b 10^{-3} \tag{38}$$

Regarding the base compartments, the equations used for evaluating the material balances are given by

$$\frac{\partial Q_b C_{Na^+,b}}{\partial x} = b J_{tot,Na^+,b} \tag{39}$$

$$\frac{\partial Q_b C_{Cl^-,b}}{\partial x} = b J_{tot,Cl^-,b} \tag{40}$$

$$\frac{\partial Q_b C_{OH^-,b}}{\partial x} = b (J_{tot,OH^-,b} - J_{tot,H^+,b}) \tag{41}$$

$$C_{H^+,b} = 10^3 10^{\left(-14-\log\frac{C_{OH^-,b}}{10^3}\right)} \tag{42}$$

$$\frac{\partial Q_b \rho_b}{\partial x} = (J_{tot,Na^+,b} M_{Na^+} + J_{tot,Cl^-,b} M_{Cl^-} + (J_{tot,OH^-,b} - J_{tot,H^+,b}) M_{OH^-}) b \\ 10^{-3} + G_{w,b} b + J_{tot,H^+,b} M_{H_2O} b 10^{-3} \tag{43}$$

In the present simulations, Ohmic, diffusive, osmotic and electro-osmotic fluxes are computed across the monopolar cation and anion exchange membranes. Concerning the bipolar membranes, the water dissociation reaction (during charge) and the acid/base neutralization (during discharge) are assumed to be infinitely fast, for the sake of simplicity. Moreover, it is assumed that the CEL proton and the AEL hydroxide ion transport numbers are equal to 1. Thus, only the Ohmic flux and its associated water flux are taken into account across the bipolar membrane.

2.4. Stack model

The stack is considered as a unit containing several triplets hydraulically connected in parallel. The middle-high modelling level is for the simulation of the stack. It involves two sub-models: the hydraulic model and the electrical model. Making use of CFD correlations on pressure drops, the former resolves three separate hydraulic circuits, i.e. one for each solution, consisting of spacer-filled channels connected by manifolds, thus predicting the pumping power consumption over the stack. The latter simulates the equivalent electrical circuit of the stack, including the ionic shortcut currents *via* manifolds, thus predicting the distribution of the electric current and of the electric potential throughout the stack (and the external circuit). Therefore, important electrical performance parameters can be calculated, e.g. the power produced/required (discharge/charge) by the stack and the RTE. Similarly to the triplet model, the inlet variables such as the channel inlet flow velocity and ion concentrations, are time-dependent and function of the solutions exiting the external tanks. Each time step is 100 s.

2.4.1. Hydraulic model

The simple hydraulic circuit considered for each solution is shown in Fig. 6. The hydraulic circuit is based on the assumption that the "slices" of spacer-filled channel with one single hole for inlet and one for outlet (see dashed line in Fig. 4) have an identical behavior and are fluxed by the same flow rate. Therefore, one single node within the manifolds of the hydraulic circuit in Fig. 6 represents any and all the manifolds sections downstream or upstream one channel (whose number is equal to that of the inlet/outlet holes, N_{holes})

Assuming a negligible mass density variation among the nodes, the continuity equation can be written as follows

$$Q_{c,sol,k} = Q_{c,sol,k-1} + Q_{c,k}(x = L) \tag{44}$$

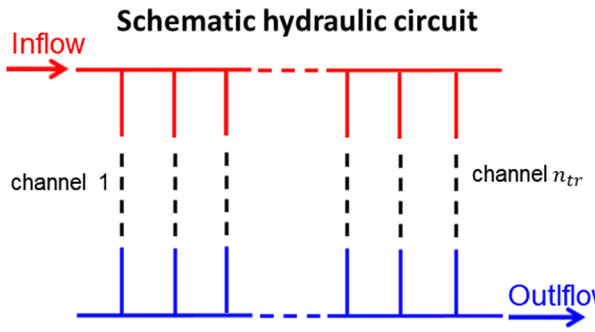

Fig. 6. Scheme of the hydraulic circuit for one of the three solutions. Vertical lines represent the channels, where pressure drops occur in the inlet/outlet regions (continuous vertical lines) and in the region with developed flow (dashed lines). Horizontal lines represent the manifolds, i.e. distributor and collector, connecting the channels.

$$Q_{c,sol,1} = Q_{sol,1}(x = L) \tag{45}$$

$$Q_{d,sol,k} = Q_{d,sol,k+1} + Q_{d,k}(x = 0) \tag{46}$$

$$Q_{d,sol,N} = Q_{sol,N}(x = 0) \tag{47}$$

where the subscripts c and d refer to the collector and the distributor, respectively, and $k = 1, 2, \cdots, N$ indicates the generic triplet, N being the total number of triplets in the stack. The validity intervals of Eqs. (44) and (46) are for k [2;N] and [1;N-1], respectively. The total feed flow rate $Q_{d,sol,1}$ is imposed in the simulations, while the total outlet flow rate $Q_{c,sol,N}$ may be higher or lower due to water transport through the membranes, computed at the triplet level.

The pressure drop within the fully developed region (vertical dashed tract in Fig. 6), i.e. the part of the spacer-filled channel where the velocity has one single component (rectilinear and parallel streamlines), is calculated by the definition of the (Darcy) friction factor

$$\Delta P_{fd,sol} = f\rho_{sol}\frac{L}{4d_{sol}}(u_{ch,sol})^2 \tag{48}$$

where f is related to the Reynolds number by the CFD correlation reported in Eq. (1), and $u_{ch,sol}$ is the mean velocity of the solution (i.e. acid, base or salt) in the channel. Note that, similarly to the channel and triplet models, the subscript k is omitted, as the equation applies indistinctly to all channels. The localized pressure losses in the inlet/outlet region of the spacer-filled channel (vertical continuous tracts in Fig. 6) $\Delta P_{l,sol}$ are calculated by the definition of the local loss coefficient

$$\Delta P_{l,sol} = k_{spacer}\frac{\rho}{2}(u_{ch,sol})^2 \tag{49}$$

where k_{spacer} is related to the Reynolds number by the CFD correlation reported in Eq. (3). The pressure drop in the small tracts of manifolds between consecutive channels (horizontal continuous tracts in Fig. 6) are calculated with a similar equation, where the flow velocity is that along the manifolds in the pertinent tract, and the loss coefficient is set by rough estimations.

The total stack pressure loss ΔP_{stack} is the sum of two contributions: the first one is obtained by the difference between the inlet to the distributor and the outlet from the collector (Fig. 6) pressures by fixing the outlet gauge pressure equal to zero. The second addend is related to further contributions to the pressure drop occurring in the distribution/collection systems among the manifolds, i.e. among the virtual ducts formed by holes in spacers gaskets and membranes.

2.4.2. Electrical model

The electrical model is devoted to quantify the currents circulating throughout the stack, including parasitic currents via manifolds. They circulate through the alternative pathways offered by manifolds and the longitudinal direction in the channels, with detrimental effects on the process efficiency, related to an average internal current different from the external one (higher in RED, lower in ED) [27]. The equivalent electric circuit solved by the electrical sub-model of stack is shown in Fig. 7.

Two longitudinal resistances are considered for each channel, while in the direction perpendicular to the membranes a voltage source and an electric resistance are considered to represent each triplet. Other electrical resistances are in the manifolds between two consecutive channels of the same solution, in the electrode compartments and in the external load for the discharge phase (BMRED). The equations system is composed of the nodes Kirchhoff's law and the Ohm's law. The following node Kirchhoff's law is applied in all the nodes of the electric circuit:

$$\sum_j I_j = 0 \tag{50}$$

where I_j is the generic electric current inputting to or outputting from each node. Positive cell currents are directed towards the cathode (i.e. negative pole during the charge, positive pole during the discharge), longitudinal currents are assumed to be positive when exiting the channels. Distributor or collector electric currents, as well as the external current are positive from left to right.

Taking into account the sources of voltage in the triplets, Ohm's law is applied as follows:

$$\Delta V_{man,sol,k} = I_{man,sol,k}R_{man,sol,k} \tag{51}$$

$$\Delta V_{x,sol,k} = I_{x,sol,k}R_{x,sol,k} \tag{52}$$

$$I_k = \frac{(\pm E_{av,k} - \Delta V_k)}{R_{av,k}} \tag{53}$$

$$I_{ext} = \frac{-U}{R_u - R_{bl}} \text{ charge phase (BMED)} \tag{54}$$

$$I_{ext} = \frac{U}{R_u + R_{bl}} \text{ discharge phase (BMRED)} \tag{55}$$

$$U_{ext} = I_{ext}R_u \tag{56}$$

where $\Delta V_{man,sol,k}$, $\Delta V_{x,sol,k}$ and ΔV_k are the k-th voltage difference over each manifold (man = c, collector, or d, distributor), the longitudinal (x = up or $down$) and the cell triplet electric resistances, respectively, U is the potential difference over the series of R_u and R_{bl} resistances, U_{ext} is the potential difference over the resistance R_u. $I_{sol,x,k}$ and $I_{sol,man,k}$ are the electric currents flowing in the flow direction and in the manifolds, $E_{av,k}$ is the average voltage generated by the cell triplet, R_u, R_{bl} and $R_{av,k}$ are the external, the blank and the average cell resistance of the k-th cell. $R_{man,sol,k}$ and $R_{x,sol,k}$ are the manifold and the longitudinal resistances

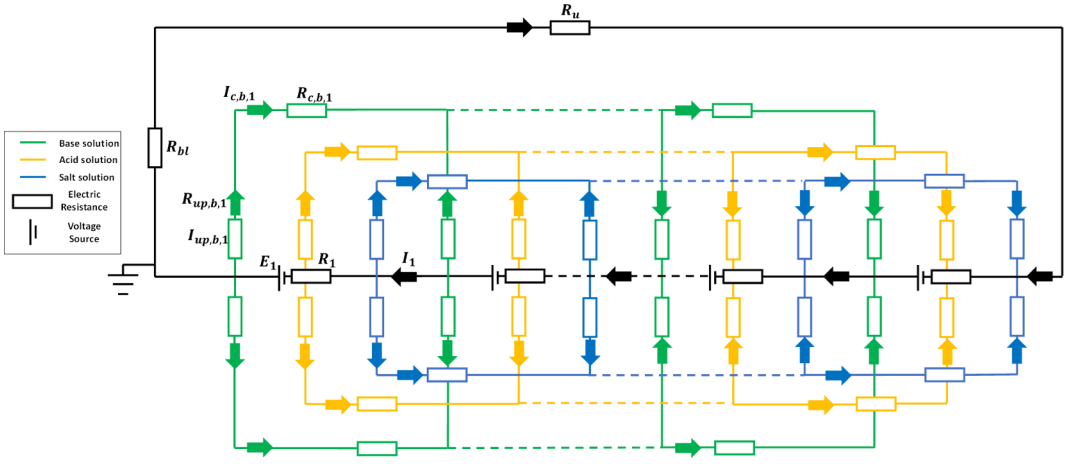

Fig. 7. Scheme of the equivalent electric circuit of the stack.

along the channel. The average triplet membrane potential $E_{av,k}$ is calculated as

$$E_{av,k} = \frac{1}{L}\int_{x=0}^{x=L} E_k(x)dx \tag{57}$$

The average cell resistance $R_{av,k}$ is given by

$$R_{av,k} = \frac{1}{L}\int_{x=0}^{x=L} R_k(x)dx \tag{58}$$

where local values are computed at the triplet level of simulation. As shown in Fig. 8, each longitudinal electric resistance along the flow direction $R_{x,sol,k}$ can be considered as the resistance along half channel length in the active area in series with the parallel of the electrical resistances out of the active area. $R_{x,sol,k}$ and $R_{man,sol,k}$ are given by

$$R_{x,sol,k} = f_s\frac{L_x/2}{d_{sol}b\sigma_{x,sol,k}} + f_s\frac{l_{oma}}{\sigma_{x,sol,k}d_{sol}d_{oma}N_{holes}} \tag{59}$$

$$R_{man,sol,k} = \frac{l_{man}}{N_{holes}\pi\frac{d_{man}^2}{4}\sigma_{man,sol,k}} \tag{60}$$

where f_s is the spacer shadow factor, L_x is half channel length, $\sigma_{x,sol,k}$ is the solution mean conductivity in the upward or downward path along the channel, l_{oma} and d_{oma} are the length and average width of the spacer regions out of the active area (i.e. in correspondence of the spacer holes), d_{man} is the diameter of the manifolds (i.e. of the spacer holes) and $\sigma_{man,sol,k}$ is the conductivity of the solution in the manifolds. l_{man} in Eq. (60) is the sum of the membranes and spacers thicknesses for a single triplet

$$l_{man} = d_{CEM} + d_{AEM} + d_{BPM} + d_a + d_b + d_s \tag{61}$$

To evaluate $\sigma_{man,sol,k}$, mass balances in the manifolds (i.e. collector and distributor) are computed. The following equations are applied

$$C_{i,man,sol,k} = \frac{C_{i,man,sol,k-1}Q_{man,sol,k-1} + C_{i,sol,k}(x=L)Q_{sol,k}(x=L)}{Q_{man,sol,k}} \tag{62}$$

$$C_{i,man,sol,1} = C_{i,sol,1}(x=L) \tag{63}$$

The validity interval of Eq. (62) is for k [2;N-1].

Volume flow rates $Q_{man,sol,k-1}$ and $Q_{sol,k}$ are already calculated by the hydraulic model.

The outlet concentrations from the stack are equal to the last collector concentrations $C_{i,c,sol,N-1}$

The gross power density GPD per triplet provided by the power supply (charge, BMED) or delivered to the external load (discharge, BMRED), defined as always positive, can be simply calculated as

$$GPD = \frac{I_{ext}U_{ext}}{NbL} \tag{64}$$

where $b{\cdot}L$ is the active area of one single membrane. Finally, the Round Trip Efficiency (RTE), which is among the main figures of merit to assess the performance of energy storage technologies, is calculated as the ratio between the (gross) energy delivered to the external load during the discharge phase and that provided by the power supply during the charge phase:

$$RTE = \frac{\int_0^{t_d} I_{ext}U_{ext}\,dt}{\int_0^{t_c} I_{ext}U_{ext}\,dt} \tag{65}$$

where t_d and t_c are the discharge and charge process times. Finally, in order to assess the impact of the parasitic current on the battery efficiency, the relative loss of RTE with respect to the ideal case without parasitic currents was calculated

$$RTE_{loss} = \left(1 - \frac{RTE}{RTE_{nopar}}\right) \tag{66}$$

in which RTE_{nopar} is the RTE computed by simulating the corresponding reference case neglecting shunt currents, carried out by a simplified model where the stack is without the parasitic branches in the equivalent electric circuit (thus it reduces to a series of identical cell resistances and electromotive forces, together with the blank resistance and the external resistance).

2.5. External hydraulic circuit and tanks model

The highest scale of the model aims at simulating mass balances and pressure drops in the external hydraulic circuits of the three solutions. It is a 0-dimensional model that can simulate the dynamic behaviour of closed-loop operations with recirculation of the solutions in the tanks. Moreover, hydraulic losses in accessory devices (e.g. valves and pumps) can be included in the calculation of the total pumping power. Dynamic mass balances within the acid and salt storage tanks can be written as follows:

$$\frac{d(\rho_{t,sol}V_{t,sol})}{dt} = Q_{t,in,sol}\rho_{t,in,sol} - Q_{t,out,sol}\rho_{t,out,k} \tag{67}$$

$$\frac{d(C_{t,HCl,sol}V_{t,sol})}{dt} = Q_{t,in,sol}C_{t,HCl,in,sol} - Q_{t,out,sol}C_{t,HCl,out,sol} \tag{68}$$

$$\frac{d(C_{t,NaCl,sol}V_{t,sol})}{dt} = Q_{t,in,sol}C_{t,NaCl,in,sol} - Q_{t,out,sol}C_{t,NaCl,out,sol} \tag{69}$$

where $V_{t,sol}$ is the solution volume in m^3, ρ_t^k is the mass density of the solution within the tank, $Q_{t,in}^k$, $Q_{t,out}^k$ are the inlet and outlet volume flow rates, respectively, $C_{t,HCl,in}^k$, $C_{t,HCl,out}^k$, $C_{t,NaCl,in}^k$, $C_{t,NaCl,out}^k$ are the inlet and outlet hydrochloric acid and the inlet and outlet sodium chloride concentrations (all expressed in mol m^{-3}).

For the base storage tank, the following equations can be written as

$$\frac{d(\rho_{t,b}V_{t,b})}{dt} = Q_{t,in,b}\rho_{t,in,b} - Q_{t,out,b}\rho_{t,out,b} \tag{70}$$

$$\frac{d(C_{t,NaOH,b}V_{t,b})}{dt} = Q_{t,in,b}C_{t,NaOH,in,b} - Q_{t,out,b}C_{t,NaOH,out,b} \tag{71}$$

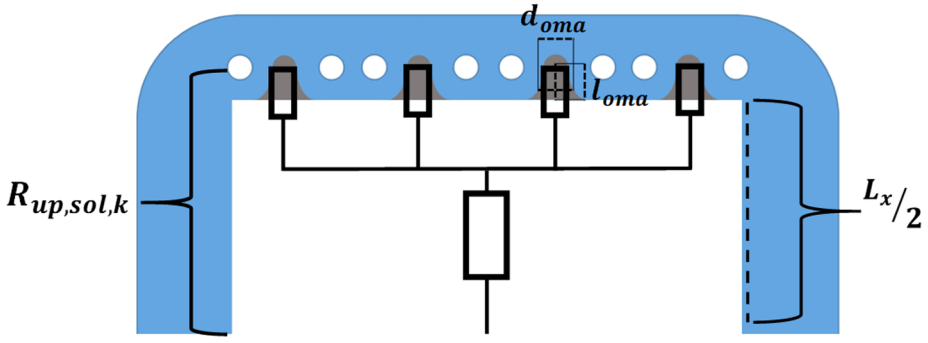

Fig. 8. Electric resistances scheme along the flow direction within the channels.

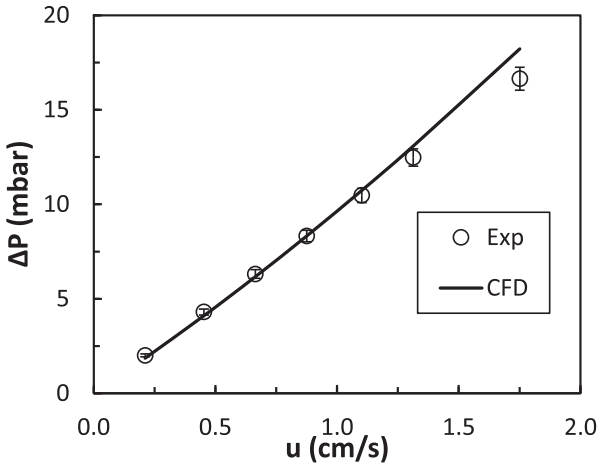

Fig. 9. Inlet-outlet pressure losses in a single spacer-filled channel flow cell as a function of the fluid velocity. Experimental data are from a previous work [41]. The main spacer features are: woven filaments, thickness of 480 μm, angle between filament of 90°, flow attack angle of 45°, pitch to height ratio of 2.42, flow path length of 10 cm (excluding divergent and convergent regions at inlet/outlet), width of 10 cm, and three inlet/outlet holes with diameter of 8.5 mm.

$$\frac{d(C_{t,NaCl,b}V_{t,b})}{dt} = Q_{t,in,b}C_{t,NaCl,in,b} - Q_{t,out,b}C_{t,NaCl,out,b} \tag{72}$$

Of course, inlet quantities for the tank correspond to outlet quantities for the stack, and *vice versa*. Therefore, $Q_{t,out,sol}$, which is imposed, corresponds to $Q_{d,sol,1}$ for a single stack. Other operations could be with single pass or with multiple passages, where a complete or partial phase (charge or discharge) occurs for the solutions flowing through the stack, which are not recirculated to the feed tank. These operating conditions can be treated as steady or sequences of steady states, adapting the previous equation for mass balances with simpler expressions.

In the hydraulic circuit of any solution, distributed pressure drops in each pipeline tract and distributed pressure drops in each singularity are given by

$$\Delta P_{dist,sol} = 8\, f_{ext}\, \frac{L_{ext}\, \rho\, Q_{t,out,sol}^2}{\pi^2 d_{ext}^5} \tag{73}$$

$$\Delta P_{loc,sol} = 8\, k_{ext}\, \frac{\rho\, Q_{t,out,sol}^2}{\pi^2\, d_{ext}^4} \tag{74}$$

in which f_{ext}, L_{ext} and d_{ext} are the friction factor, the length, and the diameter of the generic tract, and k_{ext} is the local loss coefficient of the generic singularity (tank entry or exit, valves or fittings). When the flow is laminar f_{ext} is simply calculated as

$$f_{ext} = \frac{64}{Re_{ext}} \tag{75}$$

otherwise f_{ext} is calculated following the well known Blasius equation,

$$f_{ext} = 0.316\, Re_{ext}^{0.25} \tag{76}$$

The total pressure drop $\Delta P_{tot,sol}$ in each of the three hydraulic circuits is obtained by the sum of the stack and the external parts, as follows.

$$\Delta P_{tot,sol} = \Delta P_{stack} + \Delta P_{dist,sol} + \Delta P_{loc,sol} \tag{77}$$

Then the pumping power density is given by,

$$PPD = \frac{\Delta P_{tot,a} Q_{tot,a} + \Delta P_{tot,b} Q_{tot,b} + \Delta P_{tot,s} Q_{tot,s}}{\chi\, N\, b\, L} \tag{78}$$

where χ is the pump efficiency. $Q_{tot,sol}$ are the total inlet flow rates to the stack distributor per each solution.

The net power density is calculated as

$$NPD = GPD \pm PPD \tag{79}$$

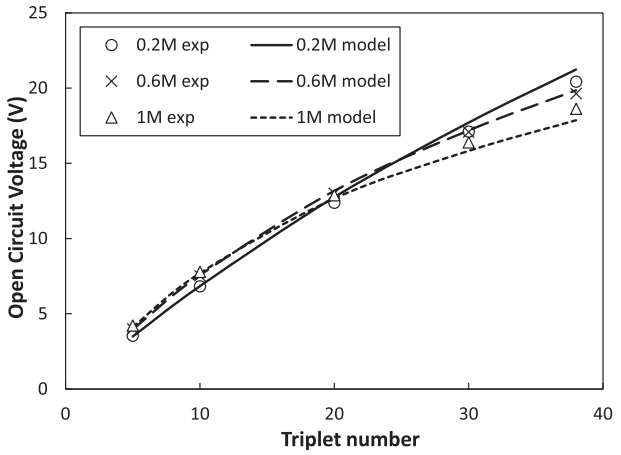

Fig. 10. OCV as a function of the triplets number in 10 × 10 cm^2 stacks with Fumatech FAB, FKB and FBM membranes. Inlet concentrations: salt compartment NaCl 0.25 M, acid and base compartments 0.2 M, 0.6 M and 1 M HCl and NaOH. Flow velocity = 0.5 cm s^{-1}.

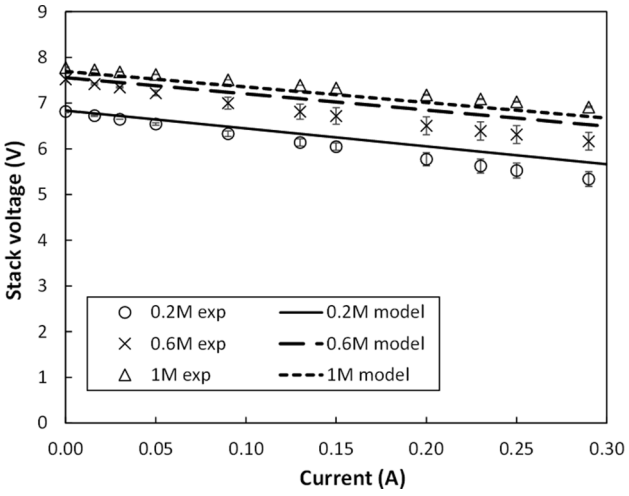

Fig. 11. Stack voltage as a function of the external current in BMRED (discharge phase) in a ten-triplet 10 × 10 cm^2 stack with Fumatech FAB, FKB and FBM membranes. Inlet concentrations: salt compartment NaCl 0.25 M, acid and base compartments 0.2 M, 0.6 M and 1 M HCl and NaOH. Flow velocity = 0.5 cm s^{-1}.

where the sign of *PPD* depends on the operating mode of the battery (i.e. − for discharge and + for charge).

3. Experimental

The lab-scale setup (FT-ED-100, purchased from Fumatech BWT Gmbh, Germany) was equipped with commercial ion-exchange membranes: fumasep® FAB as AEM, fumasep® FKB as CEM and fumasep® FBM as BPM. The stack was assembled with a number of triplets (repetitive units) from 5 to 38. The membrane active area was 10 × 10 cm^2 and PVC/ECTFE woven spacers (thickness = 480 μm) were used to create the channel between adjacent membranes. Spacers had three inlet/outlet holes per channel and the hole diameter was 8.5 mm. Two DSA-type electrodes were used in the end-compartments to convert ionic fluxes into electric fluxes (areal blank resistance of 72 Ω cm^2). A cross-flow arrangement was adopted for feeding solutions that were prepared by using demineralized water, NaCl (NaCl 99.7% ChemSolute), HCl (37% Merck) and NaOH (98–100% Honeywell Fluka). The electrode rinse solution was an aqueous solution 0.5 M in $FeCl_2/FeCl_3$ (99% ChemSolute) and 0.6 M in HCl. Peristaltic pumps

(BT601S, Lead Fluid Technology, CO LTD, China) were used for feeding all the solutions (fluid velocity in the channels of ~0.5 cm/s) in single-pass (steady conditions). All the measurements have been carried out at room temperature (~20 °C). A BK Precision 8540 DC Electronic Load was used for BMRED measurements and a BK Precision 1902 DC Power Supply for BMED experiments, both operating in galvanostatic mode. All the experiments were re-tested at least two times to verify their reliability.

4. Results and discussion

Model predictions have been compared with experimental results for validation purposes. Then, the model was used to perform a sensitivity analysis of the process performance.

4.1. Model validation

CFD predictions of inlet-outlet pressure drops in spacer-filled channels were validated against the experimental data of a previous work [41]. The results reported in Fig. 9 show a good agreement (average discrepancy of ~4%).

The process model was then validated against experimental data collected by the apparatus described in Section 3. Fig. 10 shows the Open Circuit Voltage (OCV) values measured with AB-FB stacks as a function of the number of triplets.

Fig. 10 curves differ for the inlet concentration of HCl and NaOH streams (i.e. 0.2 M, 0.6 M and 1 M) with a fixed NaCl concentration in the salt compartments. Experimental OCV were re-tested at least two times. Error bars were hidden since the average error (equal to 16 mV) is negligible compared to the voltage values. It is worth noting that the OCV increases linearly for stacks with 5–10 triplets, but then OCV deviates from linearity. This phenomenon is due to the ionic shortcut currents *via* manifolds whose effect is visible by using a high number of triplets, as predicted from the model. In fact, calculated data fit well the experimental ones, regardless of acid/base solution concentration (maximum discrepancy 4.3%).

Fig. 11 illustrates the comparison between experimental results and model predictions of the I-V curves in the presence of an electric current flowing in the external circuit as a function of the inlet acid/base concentration.

The experimental data present high reproducibility since the reported maximum deviation with the test-retest process is lower than 3.1%.

Moreover, even in closed circuit condition, the outcomes provided by the simulation tool are in good agreement with the experimental data (maximum discrepancy 6.9%). In BMRED (i.e. the discharge phase of the AB-FB), the maximum current was prudently fixed at 0.3 A (i.e., current density = 30 A/m^2). In fact, at very high current density, the amount of water produced by the neutralization reaction carried out in the interlayer of the bipolar membrane is so high that could lead to the delamination of the membrane. Thus, we recorded I-V curves not exceeding 0.3 A to avoid any bipolar membranes damage.

The simulation of the BMED process (i.e. the charge phase of the AB-FB) was validated by comparing experimental results and numerical simulations for a stack fed with 0.25 M NaCl in each compartment cell (i.e. acid, base or salt) or fed with 0.2 M HCl and NaOH streams in the acid and base compartments, respectively (Fig. 12).

The same test-rig unit of the BMRED tests was used for BMED experiments. The collected data showed high repeatability with a maximum error of 2.8%.

Comparison with experimental data shows that model outcomes fit well the experiments, with a maximum discrepancy of 7.4% found for the tests performed with NaCl only. This difference is likely due to an under-estimation of the cell resistance. Model prediction exhibits a very small variation compared with the experimental data (0.8%) in the case of 0.2 M HCl and NaOH fed in the acid and base compartments.

4.2. Sensitivity analysis

The developed multi-scale model was used to perform a sensitivity analysis to assess the impact of the main detrimental phenomena in the battery on the process efficiency. Three important aspects were identified to be possible detrimental phenomena of the flow battery: (i) energy spent for pumping, (ii) concentration polarization in the boundary layers, and (iii) ionic shortcut currents *via* manifolds. Each aspect will be separately addressed in the following sub-sections.

All the simulations were performed fixing the geometrical features, the membrane properties and the initial volume and concentration of the solutions in the charge phase at the values reported in Table A.2. The flow velocity, the number of triplets, the external current, and the manifolds diameter were let to vary.

In most cases, a round trip analysis for a single cycle of charge/discharge was simulated. The battery is considered charged (100% state of charge, SOC) once the hydrochloric acid concentration in the acid tank reaches 1 M. At that point, the model switches the operating mode from charge to discharge. The latter ends when the hydrochloric acid concentration in the acid tank becomes again 0.05 M (0% SOC).

4.2.1. Energy spent on pumping

Concerning the energy spent for pumping, Fig. 13a reports the GPD and NPD values averaged over the charge phase as a function of the mean flow velocity within the channels.

It can be observed that while the GPD trend is slightly decreasing with the mean flow velocity, the NPD exhibits an increasing trend. On the contrary, during discharge (Fig. 13b), by increasing the velocity, GPD tends to a *plateau* value around 18.2 W m^{-2}. Instead, the higher the mean flow velocity, the lower the NPD. In both steps (i.e. charge and discharge), the increase of the mean flow velocity causes mainly a flattening of the ion concentration profiles along the channels. This leads triplet potential values averaged over the whole length to be lower during charge and higher during discharge. As a consequence, GPD decreases during charge and increases during discharge (although slightly). Other possible effects of the fluid velocity on the GPD are related to polarization phenomena, as will be discussed in Section 4.2.2. On the other hand, the NPD exhibits an opposite yet more marked trend. In fact, the rise of the pumping power density with the mean flow velocity prevails on the variation of the GPD leading to an increase of the NPD during charge and a reduction during discharge. Nevertheless, the PPD, given by the difference between GPD and NPD, appears to be

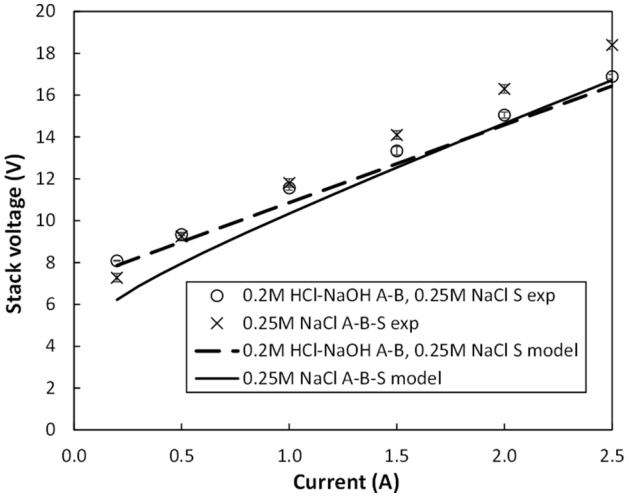

Fig. 12. Stack voltage as a function of the external current in BMED (charge phase) in a ten-triplet 10 × 10 cm^2 stack with Fumatech FAB, FKB and FBM membranes. Inlet concentrations: 0.25 M NaCl stream in all the compartments or 0.2 M HCl and NaOH streams in the acid and base compartments and 0.25 M NaCl in the salt compartment. Flow velocity = 0.5 cm s^{-1}.

Table A2
Inputs of the multi-scale model for the sensitivity analysis.

Geometrical features				
Spacer length		cm	25	
Spacer width		cm	25	
Spacer thickness		μm	475	
N° spacer holes		–	7	
Membrane properties				
		AEM	CEM	BPM
Thickness	μm	130	130	190
Areal resistance	Ω cm^2	7	6	13
H^+ diffusivity	m^2 s^{-1}	2.0E−11	0.7E−11	–
Na^+ diffusivity	m^2 s^{-1}	1.6E−11	0.5E−11	–
Cl^- diffusivity	m^2 s^{-1}	1.7E−11	0.6E−11	–
OH^- diffusivity	m^2 s^{-1}	1.9E−11	0.6E−11	–
Fixed charge group	mol m^{-3}	5000	5000	–
Initial conditions of the solutions in BMED (charge)				
$C_{t,HCl,a,out}$	mol m^{-3}	50		
$C_{t,NaCl,a,out}$	mol m^{-3}	250		
$C_{t,HCl,s,out}$	mol m^{-3}	10		
$C_{t,NaCl,s,out}$	mol m^{-3}	500		
$C_{t,NaOH,b,out}$	mol m^{-3}	50		
$C_{t,NaCl,b,out}$	mol m^{-3}	250		
$\frac{V_{t,a}}{N}$	l	0.75		
$\frac{V_{t,s}}{N}$	l	4.5		
$\frac{V_{t,b}}{N}$	l	0.75		
R_{bl}	Ω cm^2	72		

relatively small (some % of GPD), thus suggesting that the energy lost for pumping does not represent a major issue for the present system. However, real systems may require larger pumping powers, due to geometrical irregularities in the stack, effects of tightening, clogging issues, and other "non-ideal" features which cannot be included in the simulations.

4.2.2. Concentration polarization effects

Concerning the polarization phenomenon, the variation of the triplet electromotive force η_{BL} was assessed. As shown by the example reported in Fig. 14, the highest values of η_{BL}, both in absolute and in relative terms, occur during the charge phase and are higher at lower distances from the channel inlet.

At the initial point of charge, the acid and base bulk concentrations in the feed solutions are the lowest, thus the voltage variation due to concentration polarization is the highest. In particular, the lower the mean concentration of the feedwater solutions, the lower the polarization factors [42]. On the other hand, at the early point of discharge, the opposite happens and the lowest values of boundary layer voltage drop are obtained. Overall, concentration polarization accounts for less than 3% of the triplet electromotive force (E) during charge and around 0.2% during discharge, thus resulting in a small contribution to the reduction of the process efficiency. As a consequence, the polarization phenomena are not an issue for the AB-FB in the investigated operating conditions. However, larger effects are expected at higher current densities, which should be used in the operation of improved devices.

4.2.3. Ionic shortcut currents

In order to analyze the distribution of the electric current within the stack, due to the ionic shortcut currents *via* manifolds, Fig. 15 shows, for the charge step, the distribution triplet by triplet of the ratio between the manifolds current (i.e. collectors and distributors shunt for each compartment cell) and the cell current at four different external currents: 30, 100, 150 and 200 A m^{-2}.

Fig. 15 shows how the effect of the leakage currents through the manifolds can be significant. By setting an external current equal to 30 A m^{-2} (Fig. 15a), the maximum shunt currents in the manifolds of the three solution are ~50% of the cell triplet current. By increasing the external current, the ratio of the local current leakage through the manifolds to the cell triplet current decreases (Fig. 15b and c), and at 200 A m^{-2}, it accounts for ~6%.

Similar outcomes were obtained for the discharge (Fig. 16): the higher the external current, the lower the importance of the parasitic currents relative to the cell one. When no external current flows through the external circuit (open circuit condition), this phenomenon is present with the largest effects and would cause a "self-discharge" of the battery by consuming uselessly the pH gradient stored in the acid and base solutions.

These results suggest that higher external currents can be beneficial in order to increase the battery efficiency. Therefore, a specific simulations set was performed in order to investigate this aspect. The simulation results are reported in Fig. 17. At current densities higher than ~150 A m^{-2} in both phases, the loss of RTE due to shunt currents is less than 10%. However, the current density may be significantly limited by other phenomena and / or constraints, e.g. by delamination issues occurring in real BPMs. Considering a "safe" current density in the discharge phase equal to 30 A m^{-2}, with a current density in the charge phase within the range 100–200 A m^{-2}, the RTE lost due to parasitic currents spans between ~25% and ~35%

Parasitic currents are significantly affected also by geometrical features. Among them, the manifolds diameter has important effects on the electrical resistance of the parasitic pathways, thus affecting the RTE, as shown in Fig. 18a. In particular, the RTE increases from ~17%

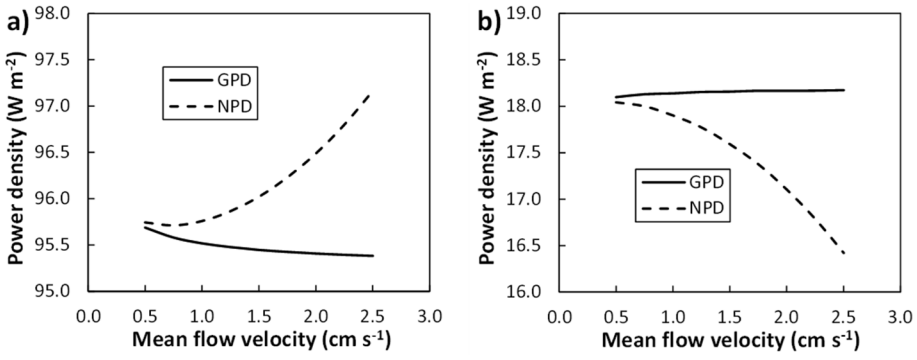

Fig. 13. Average gross power density (GPD) and net power density (NPD) for charge a) and discharge b) as functions of the mean flow velocity in the channels for stacks equipped with 40 cell triplets, spacer with inlet/outlet holes diameter of 6 mm. Charge external current of 100 A m^{-2} and discharge external current of 30 A m^{-2}. The distance between the two curves represents the pumping power density (PPD).

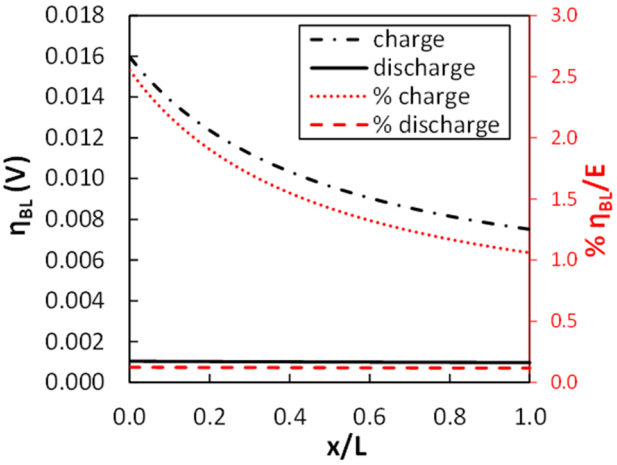

Fig. 14. Variation of triplet electromotive force due to concentration polarization in the boundary layers for the 1st triplet at the initial point of charge (SOC = 0%) or discharge (SOC = 100%), as a function of the non-dimensional coordinate along the channel. Stack equipped with 40 cell triplets, spacer with inlet/outlet hole diameter of 6 mm. Charge external current of 100 A m^{-2} and discharge external current of 30 A m^{-2}.

to ~40% by reducing the manifolds diameter from 6 mm to 2 mm. On the other hand, small manifolds may accentuate other detrimental phenomena, e.g. pressure drops, flow maldistribution and differential pressures between the channels with consequent solution leakages, or practical problems in stack assembling.

Another important stack feature is the number of triplets, as shown in Fig. 18b. The RTE exhibits an increasing trend at low values of the repetitive units number, reaching a maximum value of ~46% when the battery is assembled with 5 triplets. This behavior is due to the relative effect of the voltage drop due to the blank resistance. Then, a reduction of the RTE can be observed in stacks with a higher number of triplets, where the effects of shunt currents prevail, thus dissipating a larger portion of energy in both the cycle phases.

5. Conclusions

This work presents for the first time a process model able to predict the performance of Acid/Base flow batteries based on the reversible electrodialytic conversion of energy in stacks equipped with monopolar ion-exchange membranes and bipolar membranes. The fully integrated multi-scale model includes four sub-models for the different scales simulated, which are connected in a single tool through a hierarchical structure. The model was also supported by external information on flow and mass transfer provided by Computational Fluid Dynamics modelling.

The process model was shown to be robust and reliable by validation against experiments. Then, it was used to perform a preliminary sensitivity analysis.

Within the range of the geometrical features and operating conditions investigated (i) energy spent on pumping had a small effect on the Net Power Density, (ii) concentration polarization in the boundary layer was not an issue, while (iii) the ionic short circuit currents *via* manifolds appeared to be the most detrimental phenomena. On the other hand, pressure drops may be larger in real systems, due to

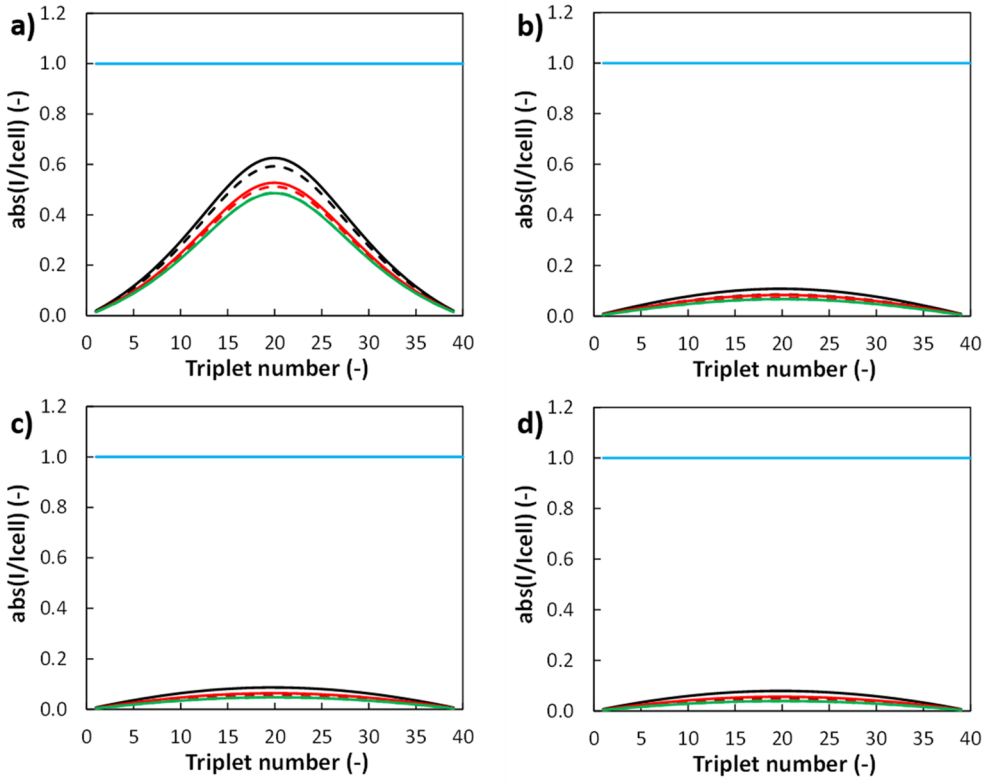

Fig. 15. Ratio between the manifolds currents and cell currents as a function of the cell-triplet position within the stack for an external current density of 30 A m^{-2} a), 100 A m^{-2} b), 150 A m^{-2} c) and 200 A m^{-2} d) during charge. I_k is the cell-triplet current, $I_{d,a,k}$, $I_{d,b,k}$, $I_{d,s,k}$ are the acid, base and salt electric currents along the distributors, $I_{c,a,k}$, $I_{c,b,k}$, $I_{c,s,k}$ are the acid, base and salt electric currents along the collectors. 40 cell triplets, spacer with inlet/outlet hole diameter 6 mm.

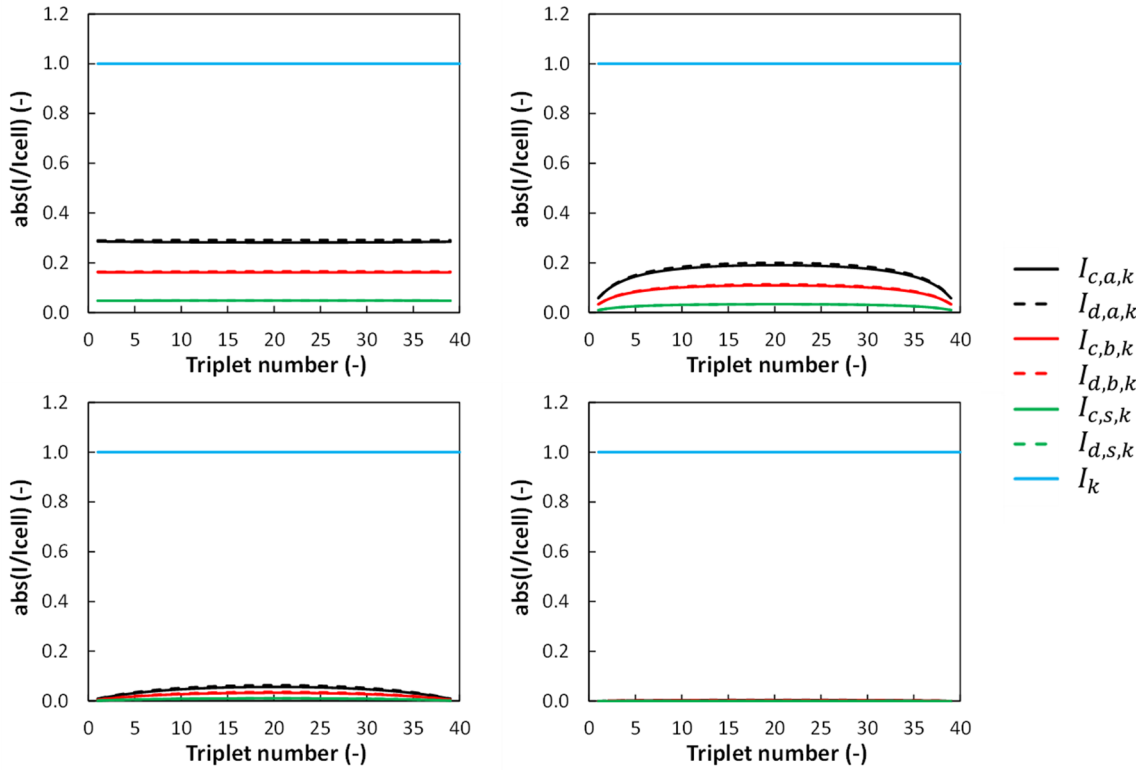

Fig. 16. Ratio between the manifolds and cell currents as a function of the cell-triplet position within the stack for open circuit conditions a), an external current density of 30 A m^{-2} b), maximum power c) and short-circuit d) during discharge. I_k is the cell-triplet current, $I_{d,a,k}$, $I_{d,b,k}$, $I_{d,s,k}$ are the acid, base and salt electric currents along the distributors, $I_{c,a,k}$, $I_{c,b,k}$, $I_{c,s,k}$ are the acid, base and salt electric currents along the collectors. 40 cell triplets, spacer with inlet/outlet hole diameter 6 mm.

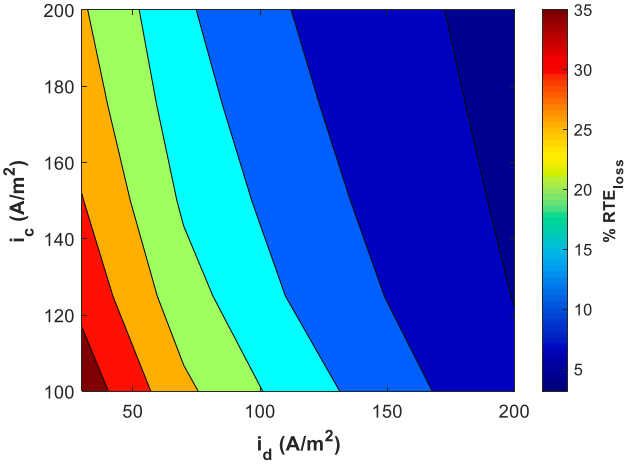

Fig. 17. Contour map of percentage of RTE loss due to the parasitic currents *via* manifolds as function of the discharge and charge external current densities. 40 cell triplets, spacer with inlet/outlet hole diameter of 6 mm.

geometrical irregularities, stack tightening, and other "non-ideal" features not included in the simulations. Moreover, concentration polarization phenomena in improved systems operated at higher current densities may have more significant effects. Interestingly, some geometrical features may affect different aspects. For example, the manifolds diameter can be crucial for the electrical resistance of the parasitic pathways. However, the use of small manifolds diameters to reduce the amount of shunt currents and their energy dissipation may pose other issues in terms of pressure drops and flow maldistribution within the channel width.

Simulation results showed also that the Round Trip Efficiency may be dramatically reduced in scaled-up stacks with a high number of triplets for the storage of large amounts of energy. Therefore, some measures have to be taken in the design of such systems in order to achieve acceptable efficiencies of the battery. For example, the use of isolated blocks with a small number of triplets can be suggested.

Finally, this original simulation tool will orient to the identification of the optimal design and the best operating conditions in order to maximize the battery performance.

CRediT authorship contribution statement

A. Culcasi: Visualization, Writing - original draft, Software, Methodology. **L. Gurreri:** Conceptualization, Methodology, Writing - review & editing. **A. Zaffora:** Investigation. **A. Cosenza:** Investigation. **A. Tamburini:** Project administration, Conceptualization, Validation, Methodology, Writing - review & editing, Supervision. **G. Micale:** Project administration, Funding acquisition.

Declaration of Competing Interest

The authors declare that they have no known competing financial interests or personal relationships that could have appeared to influence the work reported in this paper.

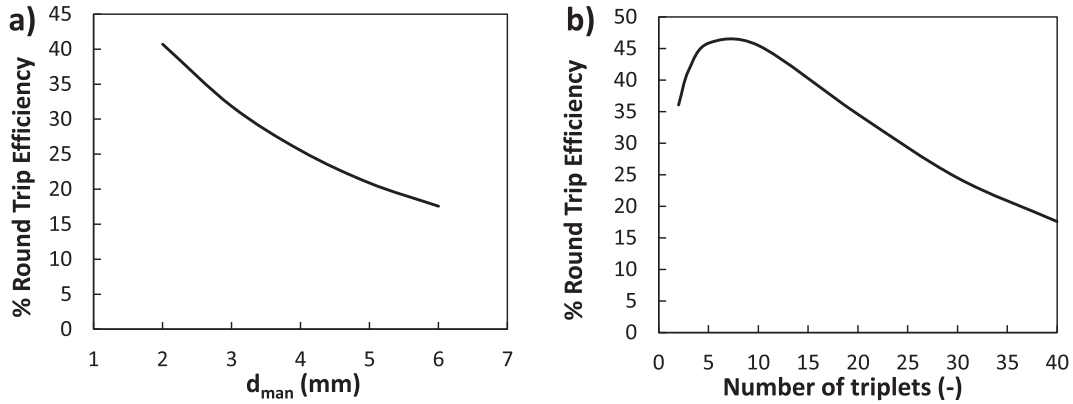

Fig. 18. Round trip efficiency as a function of the manifolds diameter for a stack mounting 40 cell triplets a), and of the number of triplets for a manifolds diameter of 6 mm b). Charge external current of 100 A m^{-2} and discharge external current of 30 A m^{-2}.

Acknowledgments

This work was performed in the framework of the BAoBaB project (*Blue Acid/Base Battery: Storage and recovery of renewable electrical energy by reversible salt water dissociation*). The BAoBaB project has received funding from the European Union's Horizon 2020 Research and Innovation program under Grant Agreement no. 731187 (www.baobabproject.eu).

Appendix A. Correlations for the physical properties of electrolyte solutions and ion-exchange membranes

For the generic physical property obtained by OLI studio, correlations assume the following general expression

$$\zeta_{sol} = k_{\zeta,sol,1} C_{i,sol} + k_{\zeta,sol,2} C_{j,sol} + k_{\zeta,sol,3} \quad (A.1)$$

where ζ_{sol} is the considered physical property ζ (i.e. electrical conductivity σ, dynamic viscosity μ or ions diffusivity D) in the solution *sol* (i.e. acid, base or salt), $k_{\zeta,sol,1}$, $k_{\zeta,sol,2}$ and $k_{\zeta,sol,3}$ are the regression coefficients, C_i is the molar concentration of the ion i, and C_j is the molar concentration of the ion j, expressed in mol m^{-3} (see Table A.1). All the regression coefficients are computed at 25 °C.

References

[1] Zappa W, Junginger M, van den Broek M. Is a 100% renewable European power system feasible by 2050? Appl Energy 2019;233–234:1027–50. https://doi.org/10.1016/j.apenergy.2018.08.109.

[2] Aneke M, Wang M. Energy storage technologies and real life applications – A state of the art review. Appl Energy 2016;179:350–77. https://doi.org/10.1016/j.apenergy.2016.06.097.

[3] Luo X, Wang J, Dooner M, Clarke J. Overview of current development in electrical energy storage technologies and the application potential in power system operation. Appl Energy 2015;137:511–36. https://doi.org/10.1016/j.apenergy.2014.09.081.

[4] Zeng Y, Yang Z, Lu F, Xie Y. A novel tin-bromine redox flow battery for large-scale energy storage. Appl Energy 2019;255:113756https://doi.org/10.1016/j.apenergy.2019.113756.

[5] Wei L, Zeng L, Wu MC, Fan XZ, Zhao TS. Seawater as an alternative to deionized water for electrolyte preparations in vanadium redox flow batteries. Appl Energy 2019;251:113344https://doi.org/10.1016/j.apenergy.2019.113344.

[6] Díaz-Ramírez MC, Ferreira VJ, García-Armingol T, López-Sabirón AM, Ferreira G. Environmental assessment of electrochemical energy storage device manufacturing to identify drivers for attaining goals of sustainable materials 4.0. Sustainability 2020;12:342. https://doi.org/10.3390/su12010342.

[7] Kingsbury RS, Chu K, Coronell O. Energy storage by reversible electrodialysis: The concentration battery. J Memb Sci 2015;495:502–16. https://doi.org/10.1016/j.memsci.2015.06.050.

[8] van Egmond WJ, Saakes M, Porada S, Meuwissen T, Buisman CJN, Hamelers HVM. The concentration gradient flow battery as electricity storage system: Technology potential and energy dissipation. J Power Sources 2016;325:129–39. https://doi.org/10.1016/j.jpowsour.2016.05.130.

[9] Campione A, Gurreri L, Ciofalo M, Micale G, Tamburini A, Cipollina A. Electrodialysis for water desalination: A critical assessment of recent developments on process fundamentals, models and applications. Desalination 2018;434:121–60. https://doi.org/10.1016/j.desal.2017.12.044.

[10] Gurreri L, Cipollina A, Tamburini A, Micale G. Electrodialysis for wastewater treatment—Part I: Fundamentals and municipal effluents. In: Basile A, Comite A, editors. Curr. Trends Futur. Dev. Membr., Amsterdam: Elsevier; 2020, p. 141–92. https://doi.org/10.1016/B978-0-12-816823-3.00007-1.

[11] Gurreri L, Cipollina A, Tamburini A, Micale G. Electrodialysis for wastewater treatment—Part II: Industrial effluents. In: Basile A, Comite A, editors. Curr. Trends Futur. Dev. Membr., Amsterdam: Elsevier; 2020, p. 195–241. https://doi.org/10.1016/B978-0-12-816823-3.00008-3.

[12] Tufa RA, Pawlowski S, Veerman J, Bouzek K, Fontananova E, di Profio G, et al. Progress and prospects in reverse electrodialysis for salinity gradient energy conversion and storage. Appl Energy 2018;225:290–331. https://doi.org/10.1016/j.apenergy.2018.04.111.

[13] Tamburini A, Cipollina A, Tedesco M, Gurreri L, Ciofalo M, Micale G. The REAPower Project. In: Basile A, Curcio E, Inamuddin I, editors. Curr. Trends Futur. Dev. Membr., Amsterdam: Elsevier; 2019, p. 407–48. https://doi.org/10.1016/B978-0-12-813551-8.00017-6.

[14] AquaBattery – We give power to water. n.d. https://aquabattery.nl/ [accessed January 10, 2020].

[15] Alotto P, Guarnieri M, Moro F. Redox flow batteries for the storage of renewable energy: A review. Renew Sustain Energy Rev 2014;29:325–35. https://doi.org/10.1016/j.rser.2013.08.001.

[16] van Egmond WJ, Saakes M, Noor I, Porada S, Buisman CJN, Hamelers HVM. Performance of an environmentally benign acid base flow battery at high energy density. Int J Energy Res 2018;42:1524–35. https://doi.org/10.1002/er.3941.

[17] Gurreri L, Tamburini A, Cipollina A, Micale G. Electrodialysis applications in wastewater treatments for environmental protection and resources recovery: a systematic review on progress and perspectives. Membranes 2020;10:146.

[18] Ran J, Wu L, He Y, Yang Z, Wang Y, Jiang C, et al. Ion exchange membranes: New developments and applications. J Memb Sci 2017;522:267–91. https://doi.org/10.1016/j.memsci.2016.09.033.

[19] Guney MS, Tepe Y. Classification and assessment of energy storage systems. Renew Sustain Energy Rev 2017;75:1187–97. https://doi.org/10.1016/j.rser.2016.11.102.

[20] van Egmond WJ. Concentration Gradient Flow Batteries: salinity gradient energy systems as environmentally benign large scale electricity storage; 2018. https://doi.org/10.1192/bjp.111.479.1009-a.

[21] Zholkovskij EK, Müller MC, Staude E. The storage battery with bipolar membranes. J Memb Sci 1998;141:231–43. https://doi.org/10.1016/S0376-7388(97)00306-2.

[22] Pretz J, Staude E. Reverse electrodialysis (RED) with bipolar membranes, an energy storage system. Berichte Der Bunsengesellschaft Für Phys Chemie 2010;102:676–85. https://doi.org/10.1002/bbpc.19981020412.

[23] Kim JH, Lee JH, Maurya S, Shin SH, Lee JY, Chang IS, et al. Proof-of-concept experiments of an acid-base junction flow battery by reverse bipolar electrodialysis for an energy conversion system. Electrochem Commun 2016;72:157–61. https://doi.org/10.1016/j.elecom.2016.09.025.

[24] Xia J, Eigenberger G, Strathmann H, Nieken U. Flow battery based on reverse electrodialysis with bipolar membranes: Single cell experiments. J Memb Sci 2018;565:157–68. https://doi.org/10.1016/j.memsci.2018.07.073.

[25] Xia J, Eigenberger G, Strathmann H, Nieken U. Acid-base flow battery, based on

reverse electrodialysis with bi-polar membranes: Stack experiments. Processes 2020;8:99. https://doi.org/10.3390/pr8010099.
[26] Campione A, Cipollina A, Bogle IDL, Gurreri L, Tamburini A, Tedesco M, et al. A hierarchical model for novel schemes of electrodialysis desalination. Desalination 2019;465:79–93. https://doi.org/10.1016/J.DESAL.2019.04.020.
[27] Culcasi A, Gurreri L, Zaffora A, Cosenza A, Tamburini A, Cipollina A, et al. Ionic shortcut currents via manifolds in reverse electrodialysis stacks. Desalination 2020;485:114450https://doi.org/10.1016/j.desal.2020.114450.
[28] Home | BAoBaB; 2019. http://www.baobabproject.eu/ [accessed January 10, 2020].
[29] Battaglia G, Gurreri L, Airò Farulla G, Cipollina A, Pirrotta A, Micale G, et al. Membrane deformation and its effects on flow and mass transfer in the electro-membrane processes. Int J Mol Sci 2019;20:1840. https://doi.org/10.3390/IJMS20081840.
[30] Ciofalo M, Di Liberto M, Gurreri L, La Cerva M, Scelsi L, Micale G. Mass transfer in ducts with transpiring walls. Int J Heat Mass Transf 2019;132:1074–86. https://doi.org/10.1016/J.IJHEATMASSTRANSFER.2018.12.059.
[31] La Cerva M, Di LM, Gurreri L, Tamburini A, Cipollina A, Micale G, et al. Coupling CFD with a one-dimensional model to predict the performance of reverse electrodialysis stacks. J Memb Sci 2017;541:595–610. https://doi.org/10.1016/j.memsci.2017.07.030.
[32] Gurreri L, Tamburini A, Cipollina A, Micale G, Ciofalo M. Flow and mass transfer in spacer-filled channels for reverse electrodialysis: a CFD parametrical study. J Memb Sci 2016;497:300–17. https://doi.org/10.1016/j.memsci.2015.09.006.
[33] Laliberté M, Cooper WE. Model for calculating the density of aqueous electrolyte solutinos. J Chem Eng Data 2004;49:1141–51. https://doi.org/10.1021/je0498659.
[34] Pitzer KS, Mayorga G. Thermodynamics of electrolytes. II. Activity and osmotic coefficients for strong electrolytes with one or both ions univalent. J Phys Chem 1973;77:2300–8. https://doi.org/10.1021/j100638a009.
[35] Pitzer KS, Kim JJ. Thermodynamics of electrolytes. IV. Activity and osmotic coefficients for mixed electrolytes. J Am Chem Soc 1974;96:5701–7. https://doi.org/10.1021/ja00825a004.
[36] Kontturi K, Murtomäki L, Manzanares JA. Ionic transport processes in electrochemistry and membrane science. New York: Oxford University Press Inc.; 2008. https://doi.org/10.1093/acprof:oso/9780199533817.001.0001.
[37] Tedesco M, Hamelers HVM, Biesheuvel PM. Nernst-Planck transport theory for (reverse) electrodialysis: I. Effect of co-ion transport through the membranes. J Memb Sci 2016;510:370–81. https://doi.org/10.1016/j.memsci.2016.03.012.
[38] Jiao K, Li X. Water transport in polymer electrolyte membrane fuel cells. Prog Energy Combust Sci 2011;37:221–91. https://doi.org/10.1016/j.pecs.2010.06.002.
[39] Han L, Galier S, Roux-de BH. Ion hydration number and electro-osmosis during electrodialysis of mixed salt solution. Desalination 2015;373:38–46. https://doi.org/10.1016/j.desal.2015.06.023.
[40] Tanaka Y. Ion exchange membranes: fundamentals and applications. Amsterdam: Elsevier; 2007. https://doi.org/10.1016/S0927-5193(07)12021-0.
[41] Gurreri L, Tamburini A, Cipollina A, Micale G, Ciofalo M. Pressure drop at low Reynolds numbers in woven-spacer-filled channels for membrane processes: CFD prediction and experimental validation. Desalin Water Treat 2017;61:170–82. https://doi.org/10.5004/dwt.2016.11279.
[42] Gurreri L, Tamburini A, Cipollina A, Micale G, Ciofalo M. CFD prediction of concentration polarization phenomena in spacer-filled channels for reverse electrodialysis. J Memb Sci 2014;468:133–48. https://doi.org/10.1016/j.memsci.2014.05.058.